

MASTER THESIS

Term paper submitted in partial fulfillment of the requirements for the degree of Master of Science in Engineering at the University of Applied Sciences Technikum Wien - Degree Program Medical Engineering & e-Health

Modeling of Airflow Characteristics and Particle Deposition in Human Upper Respiratory Tract Using CFD Simulations

By: Bc. Milan Pospisil

Student Number: 2110228032

Supervisor 1: Ing. Richard Pasteka, MSc

Supervisor 2: FH-Prof. Mathias Forjan, MSc, PhD

Vienna, 17.10.2022

Declaration of Authenticity

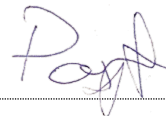
“As author and creator of this work to hand, I confirm with my signature knowledge of the relevant copyright regulations governed by higher education acts (see Urheberrechtsgesetz/ Austrian copyright law as amended as well as the Statute on Studies Act Provisions / Examination Regulations of the UAS Technikum Wien as amended).

I hereby declare that I completed the present work independently and that any ideas, whether written by others or by myself, have been fully sourced and referenced. I am aware of any consequences I may face on the part of the degree program director if there should be evidence of missing autonomy and independence or evidence of any intent to fraudulently achieve a pass mark for this work (see Statute on Studies Act Provisions / Examination Regulations of the UAS Technikum Wien as amended).

I further declare that up to this date I have not published the work to hand nor have I presented it to another examination board in the same or similar form. I affirm that the version submitted matches the version in the upload tool.”

Vienna, 17.10.2022

Place, Date

A handwritten signature in blue ink, appearing to be 'P. A.', written above a horizontal dotted line.

Signature

Kurzfassung

Das Ziel ist die Mechanismen der Luftströmung und des Partikeltransports durch die extrathorakalen Atemwege zu analysieren. Ein genaueres Verständnis dieser Attribute hilft nicht nur bei der Behandlung von Erkrankungen der Atemwege, sondern zielt auch darauf, die Anzahl der Tierversuche zu reduzieren. Für die Einschätzung wurden Computational Fluid Dynamics (CFD)-Simulation verwendet.

ANSYS wurde als führende Software verwendet, um eine Simulation verschiedener inspiratorischer Flussraten durchzuführen. An dieser Arbeit ist Large Eddy Simulation aufgrund seiner Leistung in der realen Welt beteiligt. Die Geometrie der oberen Atemwege wird aus CT-Scans erhalten, um die topologischen Daten der oberen Atemwege zu bewahren. Weiterhin wurde die Ablagerung von eingeatmeten Partikeln mit unterschiedlichen Durchmessern von 1-10 μm untersucht, was uns dabei hilft, die therapeutische Wirkung eingeatmeter Partikel besser zu verstehen. Es wurden zwei Sorten von Inhalationssimulationen durchgeführt. Zuerst Inhalation durch die Nase, die die Inhalation mit Vernebler mit Luftstromraten von 15 l / min und 30 l / min simuliert. Zweitens, durch den Mund simulierende Inhalation mit einem Trockenpulverinhalator mit einer Flussrate von 90 l / min.

Simulierte Ergebnisse zeigen, dass sich die meisten Partikel am Eingang der Nasen- oder Mundhöhle ablagern. Wenn Durchflussraten von 15 und 30 l/min verglichen wurden, ist zu sehen, dass die Partikel mit großem Durchmesser (6-10 μm) bei höherer Anfangsgeschwindigkeit in der Nasenhöhle stecken bleiben und nicht im Kehlkopfbereich erscheinen. Bei niedriger Geschwindigkeit könnten wir mehr Partikel von 6-10 μm in diesem Bereich zu finden. Die maximale Anzahl von Partikeln, die die Trachea verlassen, wurde bei einer Flussrate von 15 l/min beobachtet, was 26 % entspricht. Im Gegensatz zu 90 l/min, wo nur 13 % die oberen Atemwege verließen. Auch in Druckkonturen, die den Kehlkopfbereich beschreiben, kann ein typischer Druckabfall beobachtet werden. Dies war am signifikantesten für eine Flussrate von 90 l/min, wo der Druck vom Oropharynx zur Subglottis um 490 Pa abfiel.

Schlagwörter: Obere Atemwege, Partikelablagerung, Aerosol-Inhalation, Computational Fluid Dynamics (CFD)

Abstract

The objectives are to analyze the mechanisms of airflow and particle transport in the extra-thoracic airways. Understanding these features in greater detail not only helps in the treatment of diseases related to the respiratory tract but also aims to reduce the amount of animal testing. For the evaluation, computational fluid dynamic (CFD) simulations were utilized.

ANSYS was used as a leading software to perform a simulation of different inspiratory flow rates. In this work, Large Eddy Simulations (LES) is engaged due to its real-world performance. The geometry of the upper airways is obtained from CT scans, to preserve the topological data of the upper airways. Furthermore, the deposition of inhaled particles of varying diameters 1-10 μm was examined, helping us better understand the therapeutic effects of inhaled particles. Two types of inhalations simulations were carried out. First, inhalation through the nose, simulating the inhalation with a nebulizer with airflow rates of 15 l/min and 30 l/min. Second, through mouth simulating inhalation with a dry-powder inhaler with a flow rate of 90 l/min.

Simulated results show that most of the particles deposit at the entrance of the nasal or oral cavity. When flow rates of 15 and 30 l/min were compared, it can be seen the higher initial velocity is, the particles of large diameter (6-10 μm) are stuck in the nasal cavity and do not appear in the laryngeal region, whereas with low velocity the more particles of 6-10 μm can be found in this region. The maximum number of particles leaving the trachea was observed with a flow rate of 15 l/min, accounting for 26 %. As opposed to 90 l/min where only 13 % left the upper respiratory tract. Also, typical pressure drop can be observed in pressure contours describing the larynx region. This was most significant for a flow rate of 90 l/min where the pressure from the oropharynx to subglottis dropped by 490 Pa.

Keywords: Upper Respiratory Tract (URT), Particle Deposition, Aerosol Inhalation, Computational Fluid Dynamics (CFD) Simulation

Acknowledgements

First, I would like to thank my supervisor Ing. Richard Paštěka, MSc and Lara Alina Schöllbauer, MSc from the University of Applied Sciences Technikum Wien for their supervision and constant help with the difficulties I experienced during this scientific work.

Thanks also belong to FH-Prof. Mathias Forjan, Ph.D., MSc for providing me with an opportunity to work in a friendly team and for detailed insight into the problematics of respiration technologies.

I must not forget to thank the team that created the model of the upper respiratory tract used in this thesis.

Finally, I take this opportunity to thank my dear family for making studying possible, for their constant encouragement, support and patience.

Table of Contents

1	Introduction	6
2	Human Respiratory System	7
2.1	Anatomy and Physiology of URT	7
2.1.1	Nose	7
2.1.2	Oral Cavity	8
2.1.3	Pharynx	8
2.1.4	Larynx.....	8
2.1.5	Trachea	9
2.2	Mechanics of Breathing.....	9
2.3	Flow Rate Values.....	10
3	Aerosols.....	10
3.1	Medical Devices for Generating Aerosol	11
3.1.1	Nebulizers.....	11
3.1.2	Dry Powder Inhalers	12
3.1.3	Metered Dose Inhalers.....	12
3.2	Mechanism of Particle Deposition	12
3.2.1	Inertial Impaction.....	14
3.2.2	Gravitational Sedimentation	14
3.2.3	Interception	14
3.2.4	Electrostatic Force	14
3.2.5	Brownian Diffusion	14
3.3	Particle Deposition in URT	15
4	Computational Fluid Dynamics.....	16
4.1	Viscous Models.....	17
4.1.1	Direct Numerical Simulation	18
4.1.2	Reynolds Averaged Navier Stokes.....	18
4.1.3	Large Eddy Simulation	18
4.2	State of the Art in Modeling Airflow Characteristics in URT with CFD.....	19
5	Methods.....	24
5.1	Model Description	24
5.2	LES Governing Equations.....	26

5.2.1	Conservation of Mass	27
5.2.2	Conservation of Momentum	28
5.2.3	Conservation Energy	30
5.2.4	Discrete Phase Model for Particle Deposition	31
5.3	Meshing	32
5.4	Boundary Conditions and Initialization	34
6	Results.....	36
6.1.1	Velocity Contours.....	37
6.1.2	Pressure Contours	40
6.1.3	Particle Deposition	43
7	Discussion	48
8	Conclusion	51
	Bibliography	52
	List of Figures.....	56
	List of Tables.....	58
	List of Abbreviations	59
	Appendix A: Variability in Particle Deposition	60
	Appendix B: Turbulent Kinetic Energy Contours.....	61
	Appendix C: Wall Sheer Stress	63

1 Introduction

This thesis is dealing with the computational fluid dynamics (CFD) simulations of airflow in the upper respiratory tract (URT). The aim is to understand the natural phenomenon of the flow field of the inhaled air in the URT, and to investigate the particle deposition efficiency under different conditions. The results should contribute in developing an in-vitro URT model that could be utilized in respiratory disease treatment, and more profound investigation of the human respiratory tract.

Respiratory diseases represent a significant burden to society. Chronic respiratory diseases are the third leading global illness with the highest mortality, after cardiovascular diseases and cancer. Global mortality reaches 7 % every year [1].

Chronic obstructive pulmonary disease (COPD) and asthma were the two largest contributors to global respiratory disease burden [2]. With the COVID-19 breakout, we are now struggling even with coronavirus cases. To estimate the prevalence of chronic respiratory diseases in the population, a study was conducted in 2017, where it was found that the number has globally increased by 39,8% since 1990 [3].

New treatments that are being developed, require clinical testing before they can be used on humans, and before being introduced to mass sales. Animal testing was widely used in the past. Nowadays scientists are aiming to reduce in vivo testing on animals following the 3R principles – Replacement, Reduction, and Refinement [4]. It is unnecessary to cause animals suffering if it can be avoided. The goal is to replace animal experiments whenever possible.

This leads to exploring new alternatives to animal testing. These alternatives besides reducing animal testing also strive to improve and accelerate development of new technologies e.g., mechanical ventilators, dry powder inhalers, nebulizers [4], [5]. Alternative models can also bring an advantage over animal models because of different parameters and anatomy of the animal models – for example lung size, structure, and physiology values, which could eventually distort the results [6]. One of these alternatives can be considered upper respiratory tract model obtained from human CT or MRI scans used with an xPULM™ mechanical ventilator [7].

The objective of this work is to evaluate the airflow characteristics and particle deposition in the upper respiratory tract. The model used for CFD simulations was obtained from the CT scans of 20-year-old male. ANSYS software is used to perform simulations under varying flow rates which represent inhalation of medicaments with Dry powder inhalers and Nebulizers. This work helps to develop basic URT model, which can be further used for simulating conditions dealing with breathing problems and thus facilitating treatment of breathing deceases.

2 Human Respiratory System

2.1 Anatomy and Physiology of URT

Upper respiratory tract (URT) consists of nasal cavity, oral cavity, pharynx, larynx, and trachea. These structures can be seen in detail in Figure 1.

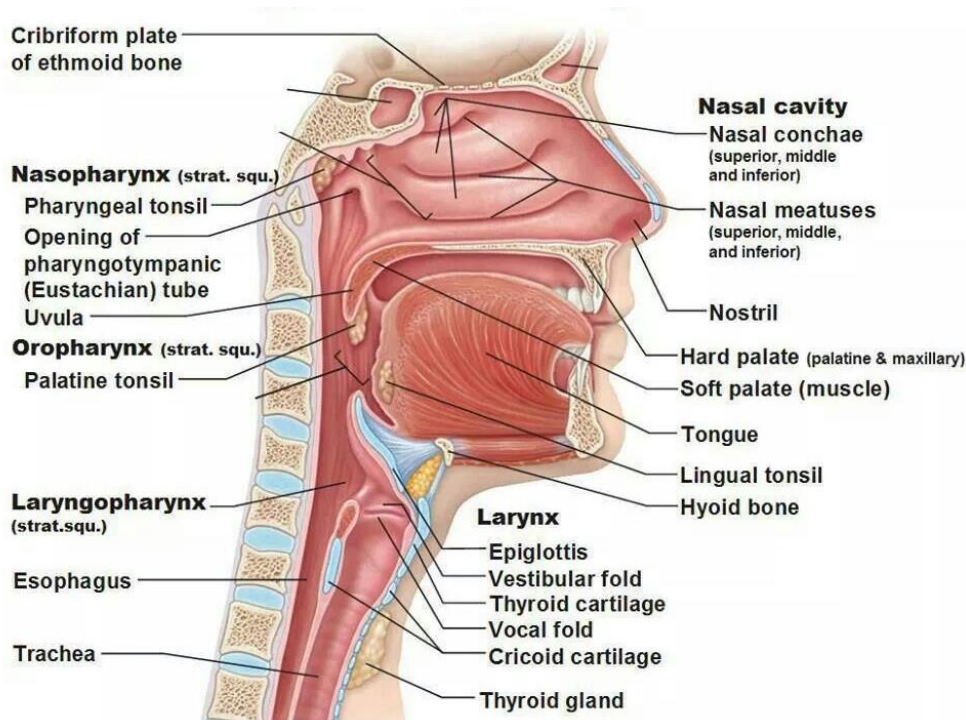


Figure 1: Anatomy of the upper respiratory tract [8].

2.1.1 Nose

The nose has external and internal part. The external part is situated in midface and consists of two nasal bones and many nasal cartilages. Inferiorly are the nares, that are openings to the nasal cavity. Further nose continues internally as nasal cavity. This part is divided by the nasal septum into left and right nostril and continues up to the nasopharynx. Nares are circled with paranasal sinuses. We distinguish sphenoid, frontal, maxillary, and ethmoidal sinuses. Typical for them is that the placement and shape differ throughout the population. The nasal cavity is separated from the oral cavity by a palate. We recognize hard palate that placed anteriorly, and soft palate that is placed posteriorly. Different routes of nasal cavity gradually join together and continues into nasopharynx. The nose plays significant role in creating ideal condition of inhaled air - approximately 37.8 °C and 100 % relative humidity. These features are required for vital functions. For example, if the air doesn't have 100 % relative humidity it will start to dry lung tissue which will in the end lead to necrosis. It also has key role in local immune defense and filtering out dangerous particles [9], [10].

2.1.2 Oral Cavity

Oral cavity consists of mouth, teeth, tongue, hard and soft palate. Oral cavity plays significant role in mechanical grinding of food using the teeth and tongue and thus further proper food digestion in stomach and intestine. Also serves as second entrance for air. The inhalation is much faster but the air is much less humidified and heated. [10] Oral cavity continues to the oropharynx where meets with nasopharynx [9].

2.1.3 Pharynx

The pharynx is about 13 cm long starting from the base of the sphenoid bone and going down to the level of C6. Pharynx is connecting the nasal and oral cavities to the esophagus and larynx. Part of the pharynx is common for the respiratory and digestive tract. The main task of pharynx is to channel air into the windpipe and further to the lungs and food into esophagus further to the stomach. Pharynx is divided into three major parts: superior part is nasopharynx, middle part is oropharynx and anterior part is laryngopharynx [9], [10], [11].

The Nasopharynx connects to nasal cavity at the superior part, where nasopharynx is attached to the base of the skull. The bottom connects to oropharynx, where can be found pharyngeal isthmus. Nasopharynx involves several important structures. One of them is soft palate that closes the entrance to nasal cavity to prevent food inhalation. Another is Eustachian tube that equalizes ear pressure. Nasopharyngeal tonsils play significant role in immune system. Oropharynx is connected to oral cavity through oropharyngeal isthmus. Tonsils are located in oropharynx to enhance the immune response [9], [10].

The laryngopharynx forms the last structure that leads air as well as food. After laryngopharynx the pipe is divided into larynx and esophagus. Crucial role in the channeling plays esophagus. The major landmark that can be seen in laryngopharynx is piriform fossa leaving little depression on either side of laryngopharynx and is a common site for impaction of swallowed sharp foreign subjects [9], [10].

2.1.4 Larynx

The larynx is located inferior to the pharynx and anterior to trachea between 3rd to 6th cervical vertebrae. Larynx consist of cartilages, muscles, and ligaments. These components performs various functions, including airway protection and phonation [9], [10].

Inferior to the pharynx is located eight rigid hyaline cartilages and one elastic cartilage. The largest of the hyaline cartilages is the thyroid cartilage, which is visible on men neck and is commonly called Adam's apple. The elastic cartilage is called epiglottis, it closes the entrance to the larynx to prevent food entering wrong pipe. Part of the mucous membrane of the larynx forms a vocal cord which are located amid of thyroid cartilage. The space between the vocal cords is called glottis. We distinguish supraglottis that is superior to glottis and subglottis that is inferior. The vocal cords can be easily recognized because of absence of blood vessels [11].

2.1.5 Trachea

The trachea is windpipe about 10-12 cm long. Trachea goes down to the level of the fifth thoracic vertebra. The trachea is rigid. Its walls are reinforced by C-shaped hyalin cartilage rings [9].

2.2 Mechanics of Breathing

The major pressures that affect pulmonary ventilation are: 1. atmospheric pressure, 2. alveolar pressure, 3. intrapleural pressure, and 4. transpulmonary pressure. Graphical representation of these pressures can be seen in Figure 2. The basic principle of breathing is that when intercostal muscles and diaphragm contract, it leads to volume changes in the lungs. And volume changes lead simultaneously to pressure changes, which lead to the flow of air to equalize the pressure [12], [13].

Atmospheric pressure is the pressure within the atmosphere on Earth. Atmospheric pressure measured at sea level is equal to 101,325 Pa or also 760 mm Hg. At an increasing altitude, the atmospheric pressure decreases. Furthermore, we define negative pressure, which refers to a pressure that is lower than atmospheric pressure, and positive pressure, which is greater than atmospheric pressure [12], [13].

Alveolar pressure is the air pressure within the alveoli, also known as the intrapulmonary pressure. Alveolar pressure fluctuates during inhalation and exhalation between approximately -1 mmHg and +1 mmHg [12], [13].

Intrapleural pressure is the pressure exerted by the air within the pleural cavity. The pleural cavity consists of visceral pleurae and parietal pleurae. Although it fluctuates during inspiration and expiration, intrapleural pressure remains approximately -4 mm Hg during calm breathing and is always slightly negative to atmospheric pressure – this characteristic keeps the lungs expanded (this can be broken during pneumothorax, which causes the lung to collapse). Intrapleural pressure becomes more negative with forced inspiration and more positive with forced expiration-but it remains in negative values [12], [13].

Transpulmonary pressure represents the difference in pressures between Alveolar pressure and Intrapleural pressure [12].

To take a breath in, the diaphragm moves down. This expands the lungs, increasing lung capacity. At the same time, this creates negative pressure within the lungs, and so air rushes into the lungs to equalize the pressure. Expiration happens mainly due to the natural elasticity of the lungs but also with the help of intercostal muscles and the diaphragm.[12], [13]. The typical breathing volume 500 mL and the frequency of breathing is 12 breaths per minute [12].

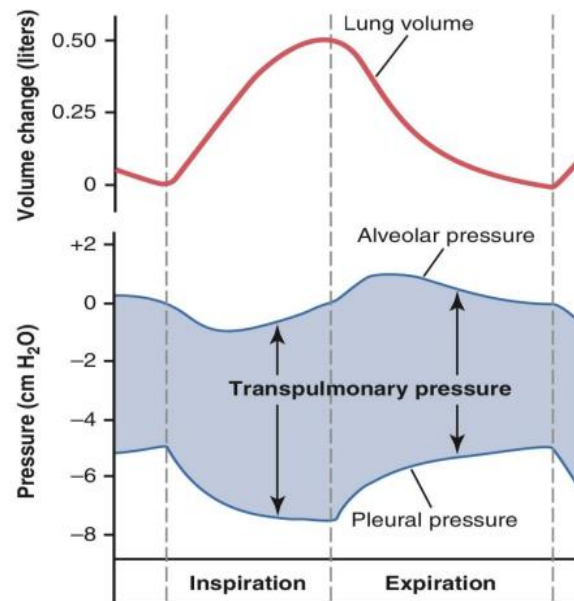


Figure 2: Changes in lung volume, alveolar pressure, pleural pressure and transpulmonary pressure during normal breathing [14].

2.3 Flow Rate Values

During the day, flow rate can change according to physical activity. We can measure 12 L/min during sleep [15]. 60 L/min during normal breathing with averages ranging from approximately 40 L/min at rest, to 286 L/min during heavy exercise. Some subjected generated maximum flow rates reaching 374 L/min [16]. Values during inhalation of medicaments with dry powder inhaler are usually around 90 l/min, and the inhalation last 1 s. Nebulizers on the other hand, works with flow rate of 15 - 30 l/min, with the duration of 2 - 2,5 s [17].

3 Aerosols

Aerosols are formed by solid or liquid particles dispersed in the air. They can be carriers of medical substances, dust, and dangerous viruses. Aerosols play a significant role in the treatment of many pulmonary diseases such as asthma or COPD. The basic parameter that influences the behavior of a particle is its size. The dispersed particles have a size of 10 nm to 100 μm [18]. Aerosols can be classified into types based on many factors. They can be classified based on the size of the particles (coarse or fine). The aerosol can be monodisperse. I.e., composed of particles of a very small size range. Or polydisperse, containing a broad spectrum of size ranges. They can also be categorized as primary (delivered into the atmosphere directly) or secondary (formed through condensation, oxidation, etc.). The five most basic classifications of aerosols are dust, fume, mist, smoke, and fog [18].

3.1 Medical Devices for Generating Aerosol

Dry powder inhalers (DPI), Metered dose inhalers (MDI) and Nebulizers are mostly used in medicine for inhalation therapy. Each of these devices has strengths and weaknesses that a doctor must consider when prescribing aerosol treatment. The success of inhalation therapy depends on several factors. First, an appropriate medication must be used. Second, the medication needs to reach the required position. And lastly, to which extent the deposition happens in this position. The last two are highly affected by the diameter of the used particles in medicine, but also how properly the inhalation was performed by the user. For this, it is necessary to train users, so they use the devices correctly. Lack of information can cause ineffective treatment [19].

There are several requirements that ideal inhaling device should meet. Firstly, the medicament that is supposed to be delivered, should be safe and effective, meaning that it should not cause any side effects to the patient, and it should help locally where the treatment is needed and avoid systematic effect. Secondly, the inhaling device needs to be easy to use and user friendly. Additionally, the inhaling device should not harm the environment. Lastly, there is high need for high quality aerosol in terms of aerosol size [20].

3.1.1 Nebulizers

Nebulizers are electrically powered machines that turn medicine from liquid form into a fine mist. The mist is propelled with compressed air through a plastic tube up to the mouthpiece or facemask, which is attached to the face. Nebulizers are easy and intuitive to use. They can be used for patients of every age and for any disease severity. In some cases, it is possible to mix more than one medication in a nebulizer and deliver them simultaneously. This can reduce the time needed for treatment with more than one drug. One of the benefits of nebulizers is the ability to use very high drug doses [21].

All that is needed for functioning is to put on a facemask and breathe normally, compared to inhalers where the breathing must be perfectly timed. With the development of nebulizers, patients do not need to visit a doctor to perform the treatment. They can also afford a home nebulizer or even portable nebulizer that runs on batteries and can fit into a briefcase [20].

There are three types of nebulizers, divided according to how the mist is generated:

1. Jet – using compressed air to disperse the liquid
2. Ultrasonic – aerosol is made through high frequency vibrations in liquid container. This creates the largest particle of all the three types
3. Mesh – liquid is pushed through a fine mesh. This type creates the smallest particles

Nebulizers have no propellants that might harm the environment and require no training to use. Nebulizers are more time-consuming. One treatment session takes up to 5-10 minutes. Furthermore, nebulizers need cleaning and servicing [22].

3.1.2 Dry Powder Inhalers

The medicine is delivered in powder form. The dry powder inhaler (DPI) doesn't have a propeller, so the patient must inhale the powder quickly and deeply with his own muscle power. When a patient breathes in, it disintegrates the powder into smaller particles. The DPI has a counter integrated into the mechanism, so the patient knows when the medication is about to run out. DPIs are quick to use and easily portable. Downside of the device is a requirement for higher inspiratory flow, approx. about 90 l/min. If the patient cannot exert such power, the device is not recommended [23].

DPIs are most suitable for adult patients with asthma and COPD. The most common errors when using DPI are exhaling into the inhaler or not enough long breath hold after inhalation. This inhaler is breath-activated, so there is no need for coordination. This is different than a metered dose inhalers that propel medication into the lungs [20].

3.1.3 Metered Dose Inhalers

Unlike the DPI, metered dose inhaler (MDI) contains a propellant that on actuation delivers a specific amount of medication to the lungs. The medication is typically stored in a solution in a pressurized canister. Actuation and inhalation must be coordinated. A common error when using MDI is that the patient launches the propeller, but he doesn't breathe in sufficiently, so the drugs stay mostly in the mouth. MDIs do not contain dose counters, so it is difficult to tell how much drug remains [21].

MDI can be used with a spacer. The spacer enables to breath in all the dose of medicine into the lungs. It is attached to the inhaler, and when the person breathes in, the medicine is slow down and is held in this chamber, so the person can breathe normally without any changing of breathing pattern, and the medicine is not lost. On the other hand, the efficiency is decreased when using a spacer compared to proper inhalation without a spacer. Firstly, because the patient doesn't breathe in with sufficient speed, the particles don't reach required position. Secondly, the particles can attach to the inner wall of the chamber, which decreases lung delivery [20].

MDIs cannot be used by people with sensitivity or cardiotoxicity to propellants. There is also higher probability compared to DPI that user will develop bad inhalation technique. MDI are harder to use because of the requirement for coordination [22].

3.2 Mechanism of Particle Deposition

Aerosols are after inhalation deposited in respiratory tract under five different factors: gravitational sedimentation, inertial impaction, diffusion, electrostatic force, and interception. These deposition mechanisms are shown in Figure 3. Particle size is the most important

factor determining in which area the particle may deposit. The dependency of particle diameter on the type of deposition is depicted in Figure 4. For microscopic particles, majority of deposition is caused by impaction due to inertia and gravitational settling. If the particle size is in nanoscale, then Brownian diffusion is another significant factor of particle deposition. Since URT inside wall is covered with mucus, the particles are very likely to get stuck when they touch the wall [24], [25].

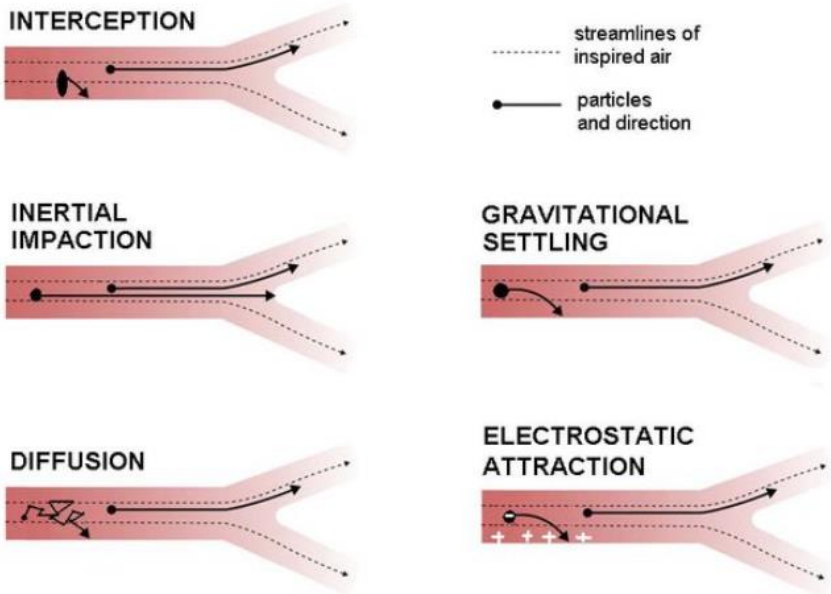


Figure 3: Different mechanisms of particle deposition [26].

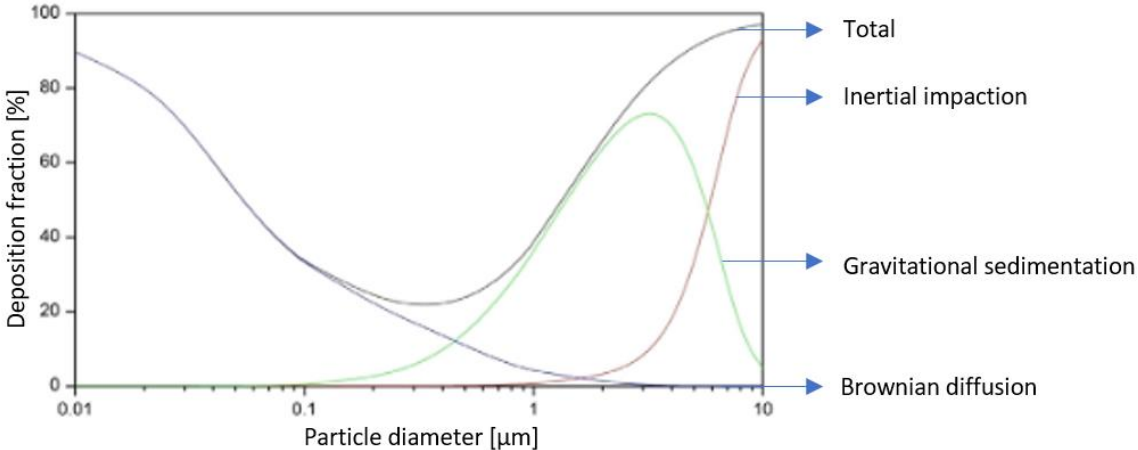


Figure 4: Particle deposition in lungs with three different types [27].

3.2.1 Inertial Impaction

It primarily affects particles larger than 5 μm in size. These particles are not able to follow sudden changes in airflow direction. With this deposition, particles are stuck after touching the obstacle that is in the way of flowing air. Inertial impaction is the most dominant way of particle deposition in URT. It's because URT is very complex and contains many folds and rapid changes in geometry, and the velocities are very high [24], [25].

3.2.2 Gravitational Sedimentation

Occurs due to the gravity force and prevails mainly in small airways and alveolar region. Possibility of gravitational sedimentation increases if the size of particles is large but drag force generated by inspiratory airflow is weak. If drag force is not powerful enough to carry particle, then such particles are likely deposited due to gravitational settling. Another factor that increase this kind of sedimentation is, if the distance between particle and wall is low [24], [25].

3.2.3 Interception

Occurs by the physical contact of the particle with the surface wall of respiratory tract. This type of sedimentation happens, when the particle is traveling near to the surface and when one edge touches the URT wall the particle becomes stuck. The main difference with inertial impaction is that in case of interception there is no need for the obstacle in the way [24], [25].

3.2.4 Electrostatic Force

Some particles carry their own electrical charge. This charged particle is then attracted to the opposite charge located on the wall of the URT. This is the main principle of particle deposition by electrostatic force. Deposition by electrostatic force occurs most in the bronchial and alveolar region where inertia force is weak and also the diameter of the tubes is getting smaller [24], [25].

3.2.5 Brownian Diffusion

Brownian diffusion affects mainly particles with sizes around 0.5 μm and less. These particles collide with other moving gas molecules. After collision, the particles bounce back, and this is what creates the irregular movement. Brownian diffusion represents the main particle deposition mechanism in alveolar region. These tiny particles are following the air stream while they are still in random motion, and so they deposit mostly by chance on the walls of URT. Very fine particles (0,01 μm), deposit in the upper parts of URT because the smaller the size of particle is the more vigorous the movement is [24], [25].

3.3 Particle Deposition in URT

Inertial impaction is the main cause of aerosol deposition in the upper airways. High velocities and rapid changes in flow direction make it difficult for particles to follow the main stream. After the particles hit the walls of the airways, they become trapped.

The larger the particle, the higher the likelihood that it will be deposited by the impaction. If the particles are very large ($>10\ \mu\text{m}$) the main area of deposition becomes the beginning of nasal or oral cavity [28]. The type of particle deposition and the amount of deposited particles is highly dependent on the particle characteristics such as particle size, overall size distribution in injection, shape, composition, surface characteristics of the wall, and charge [29]. Large particles ($>10\ \mu\text{m}$) tend to deposit in the URT particularly in the oral or nasal cavity. This means, this diameter of particles is not recommended to use in lung treatment. Small particles in the size range from 3 to 6 μm deposit mainly in the oropharynx region and in tracheal region (see Figure 5). Bronchial region on the other side is not much affected with the particle deposition. Whereas in alveolar region treatment, particles around 1 μm plays significant role [30], [31].

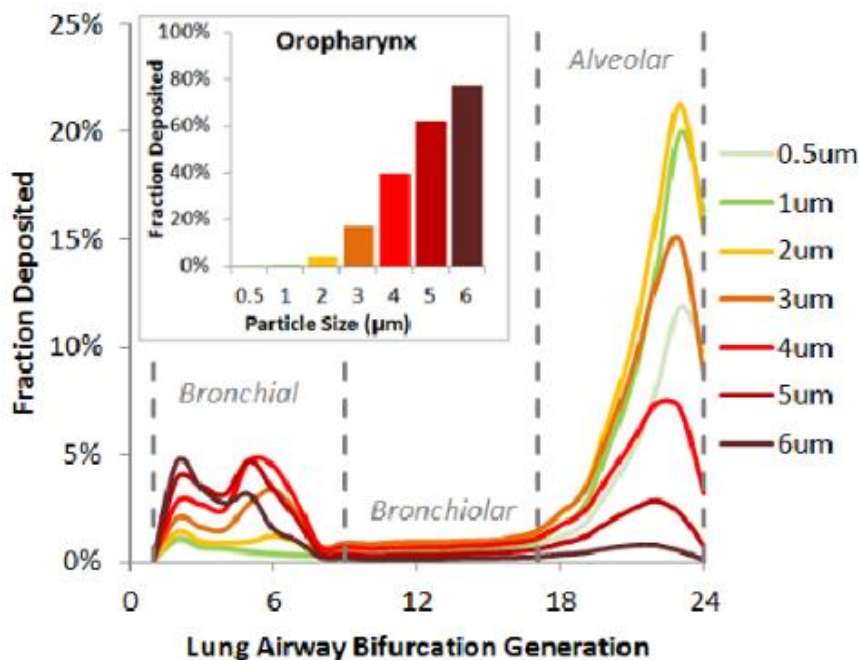


Figure 5: Lung deposition distribution for various particle sizes [32]

Particle deposition can be predicted with help of Stokes number. The Stokes number helps us determine the behavior of particles dispersed in a fluid flow. If Stokes number is less than 1 then the particles follow the streamline of the flow. If Stokes number is greater than 1, particles detach from the streamline and follow their own path, and thus the particles are very likely to be deposited [33]. Reynolds number, on the other hand, helps us predict whether the flow is laminar or turbulent. The flow in upper airways is mostly turbulent [33].

4 Computational Fluid Dynamics

Fluid dynamics (FD) is focused on describing flow of the fluids – liquid and gases. FD can be used to describe any situation where the fluids are involved – naturally, this involves every aspect of human life. FD can determine velocity and pressure, and thus the behavior of a fluid at any point in the model [34], [35].

The foundation for FD is Navier–Stokes equations. These equations date from the 19th century when Navier and Stokes came up with them independently. Most of the problems couldn't be solved back then, because in too complex geometry, the Navier–Stokes equations become difficult to solve. That is why computational-FD (CFD) takes upturn in recent years with the development of computer computational capability [34], [35].

CFD is one of the most basic methods for evaluating fluid dynamics and is classified as a numerical solution. The second is analytical, where the solution involves the calculation of an exact solution with generalized equations. This approach is very laborious and not feasible with too complex model. The third way is experimental, where the observed results are very accurate but require a specialized facility, and compared to the other two ways, is the most expensive one. Although, the results of mathematical models is sometimes necessary to verify and compare with experimental data, to evaluate if the model is representing the real world performance correctly [34], [35].

CFD is giving us a lot of flexibility of analytical method and accuracy of experimental method. With CFD simulations, researchers can evaluate the real-world performance of any model. This approach helps to reduce time and expenses spent on the development of the real-world model and allows researchers to optimize their design efficiently [34], [35].

CFD is also able to predict the particle movement in the fluid domain and particle deposition on the walls with the adoption of Discrete phase model which will be further described in chapter 5.2.4. CFD helps us better understand how airflow effect particles and what influence the particle deposition. As a result, we can for example see that 1 μm particles has very high probability to travel up to lungs with the low deposition alongside the URT. On the other way most of 10 μm particles are deposited with high probability at the entrances of nasal or oral cavities.

The basic principle of CFD is to divide the geometry into many small cells during a process called meshing, with each cell interacting with its neighbor. This procedure is necessary because we are not able to compute the Navier–Stokes equations in the whole geometry but only within the small and known structure. For this, spatial discretization is needed. CFD finds a numerical solution, which means that the computer is making guesses and the solution is found when convergence criteria is met. The finite element method (FEM), finite difference method (FDM), and finite volume method (FVM) are the three basic numerical modeling methods used for discretization [34], [35].

ANSYS implemented FVM. It is a numerical technique that transforms the partial differential Navier–Stokes equations over differential volumes into discrete algebraic equations over finite volumes (basic elements or cells in a mesh). These elements are also called control volume. Typically, they have a point at a center where the variables are stored. When computing the algebraic equations in the control volume, the interpolation function is applied to capture the differences between neighboring elements [34], [35].

Several steps are crucial in CFD computing:

1. Remove from the model overlapping regions and non-manifold geometry
2. Define inlets and outlets and walls
3. Extract the flow domain from the geometry
4. Create the elements (generate the mesh) – the geometry is discretized according to the mesh settings in the ANSYS software where fine, medium and coarse mesh can be selected
5. Establish initial conditions
6. Set the boundary condition along the edges of the mesh
7. Choose the viscous model (turbulence model)
8. ANSYS automatically transforms the partial differential equations into algebraic equations with use of FVM
9. Computer through many iterations compute the solution along all the elements until convergence criteria is met

4.1 Viscous Models

Most respiratory flows typically involve three flow types - laminar, turbulent, and transitional. In the extra-thoracic regions, Reynolds numbers range from a few hundred to values exceeding five thousand during heavy breathing [36].

The fast changes in flow regimes are difficult to calculate. The turbulence is creating vortices which can be represented in 2D like scales. With an increasing Reynolds number, the scales are getting smaller. The mixing of small and big scales is not easy to calculate. For this reason, viscous models were developed. It helps us better simulate the flow through the model. There are various viscous models available for CFD to characterize fast transitions between the laminar-transitional-turbulent flows. The Reynolds-averaged Navier–Stokes equations (RANS), large eddy simulation (LES), and direct numerical simulation (DNS). Each has its advantages and disadvantages, which have to be considered before starting the simulation [37].

4.1.1 Direct Numerical Simulation

Direct numerical simulation (DNS) is the most precise method, but extremely computationally demanding and thus, in most cases, cannot be used [37]. It is a method in which the Navier–Stokes equations are numerically solved directly using a very fine mesh (the cell number can reach up to one billion). The basic principle of DNS is to capture all the scales that are present in a particular flow. DNS can be currently applied only to very simple geometries and for low Reynolds number issues (to 1000 Re). In our case, DNS cannot be used, partly because ANSYS doesn't support this viscous model. But mainly it's because the URT model is too complex and it is not possible to find a solution [38].

4.1.2 Reynolds Averaged Navier Stokes

The Reynolds averaged Navier Stokes RANS was the most frequently used group of viscous models thanks to their capability to describe the changing flows between laminar, transitional, and turbulent flow while using little computational resources. However, today, with computer technology development, RANS is slowly pushed away with Large eddy simulation (LES) viscous model. The basic principle of RANS is time averaging i.e., velocity through all the time periods. The big differences between large and small scales are smoothed out. Obviously, lot of details is lost with this approach.

There are many subtypes of RANS on the market. One of them is SST k- ω (Shear stress transport). In this model, in addition to the conservation of mass and momentum equations, further solved turbulent kinetic energy (k) and specific dissipation rate (ω) which helps to better predict flow characteristics. However, this model is not very efficient with unsteady flow structures. [37] It has been observed that SST k- ω model was better in computing the flow characteristics in the trachea when the breathing rate was small, meaning that the flow reached only low Reynolds number. When the flow rate increased, the SST-Transition model was the best choice for the flow characteristics calculation [39].

4.1.3 Large Eddy Simulation

Currently, LES is becoming more popular method to model the airflow in the respiratory airways since it has higher capability to predict the quickly changing flows between laminar-transitional and turbulent flow. Moreover, it reveals more detailed flow structures of the mechanism of particle dispersion. The drawback of this method is its higher computational complexity compared with RANS viscous models. [37]

In DNS, all the scales are solved. In RANS, the average is made between the scales. LES is using another approach. Only the large scales are calculated, and for the small ones, a special model is implemented. Often, a low-pass filter is applied. This reduces computational complexity a lot when small scales are present, while keeping most of the information chapter. This method is used to simulate airflow and particle deposition in this thesis and will be further described in detail in 5.2.

4.2 State of the Art in Modeling Airflow Characteristics in URT with CFD

Many studies have been conducted on CFD simulation of airflow in the respiratory system throughout the past years. Either focusing on the extrathoracic airways or the whole respiration system. Earlier, many of these studies were conducted only with simplified geometry that was created in the CAD program and thus are just approximations of the real URT. Many of these studies also didn't take into consideration the nasal cavity and used only oral inlet. However, even small geometric variations have a profound effect on the results. Also, it needs to be taken into consideration that there is a large difference in geometry of URT in the human population, especially with respect to age. Nowadays, we can notice an increasing number of studies using realistic geometry that is extracted from CT or MRI scans. Only studies that use realistic geometry will be further examined since it provides better comparison for case used in this thesis.

Naseri et al. (2014) worked with URT model to simulate particle deposition of various particle sizes (2, 5, 10, 20, 30, 50 μm) under different flowrates (7, 10, 15 l/min). The model is subdivided to smaller fraction according to anatomical significance (Figure 6). In their study the key observation is that the particle deposition significantly varies as size of particles is changed, and majority of particles greater than 20 μm are not able to pass the larynx and are highly deposited in nasal cavity. Particles with diameter 50 μm are mostly deposited in vestibule of nasal cavity [40]. Deposition patterns can be seen in Figure 7.

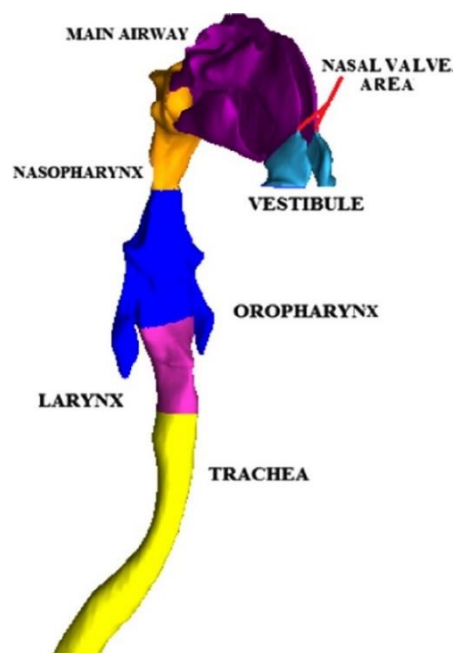


Figure 6: realistic extra-thoracic region developed by Naseri et al. (2014) [40].

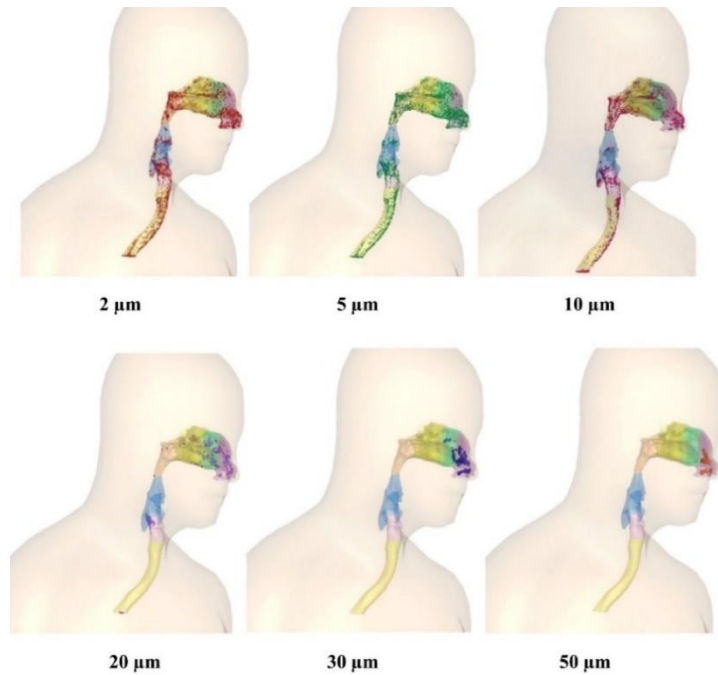


Figure 7: deposition pattern variation by particle size with flow rate of 7 l/min [40].

To verify findings in particle deposition research along with flow rate characteristics **Liu et al. (2022)** applied LES method to inspect the inhalation process through nasal cavity with flow rates of 15 l/min and 30 l/min. Particle diameter of 1 μm , 10 μm and 20 μm are used to evaluate particle deposition. [41] They achieved very similar results as Naseri et al. (2014). Chosen cross sections are depicted in Figure 8. Velocity contours in these cross sections in Figure 9. Results from the particle deposition investigation re depicted in Figure 10 and Figure 11.

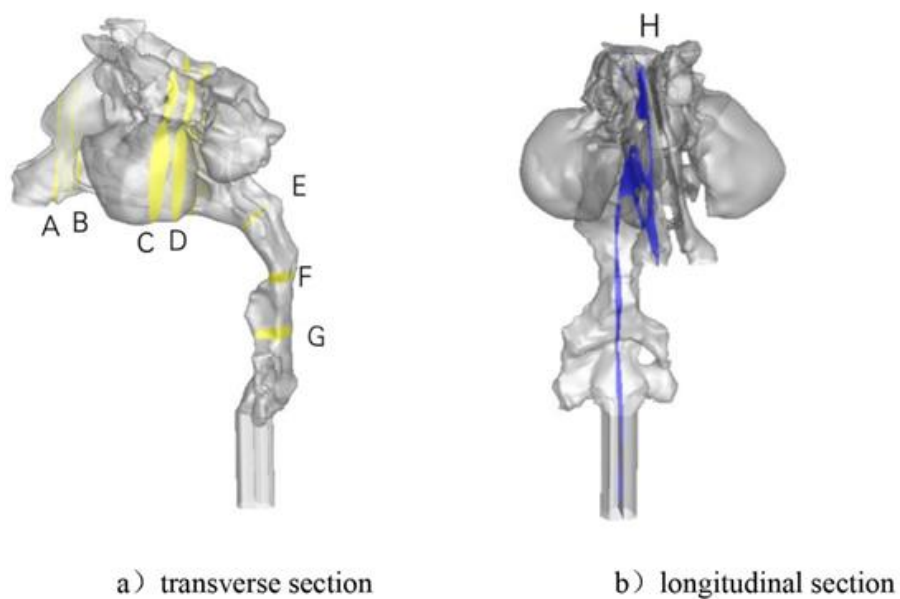
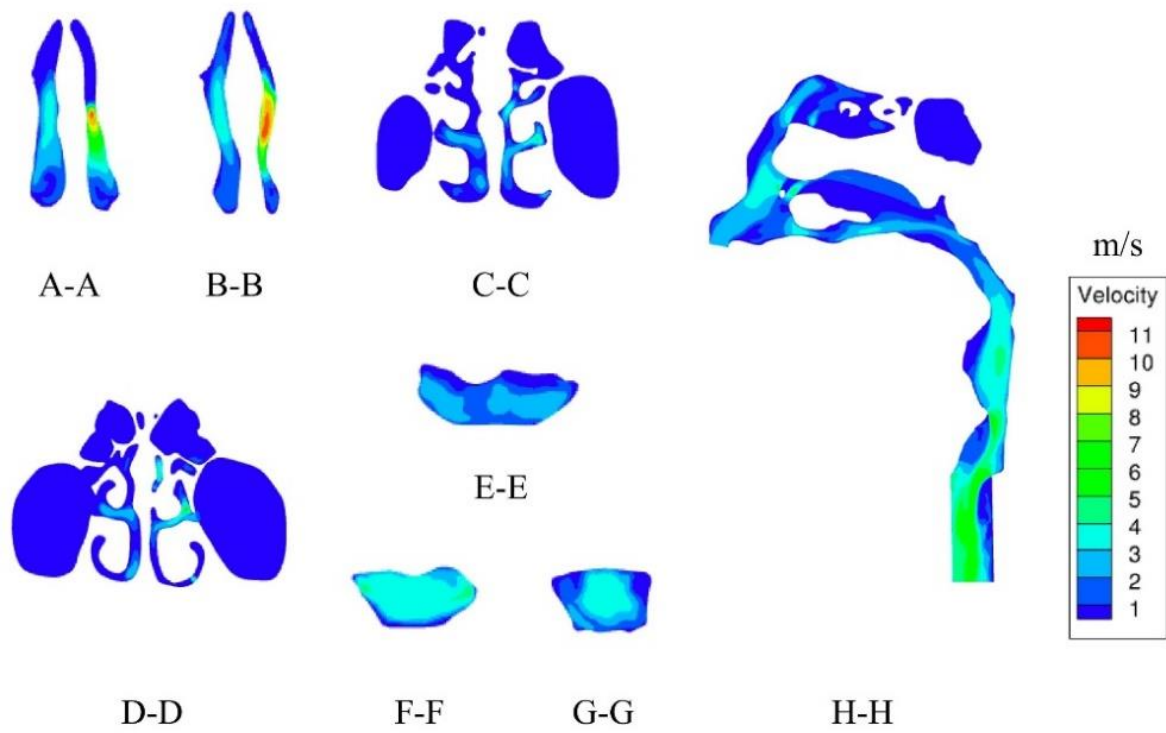
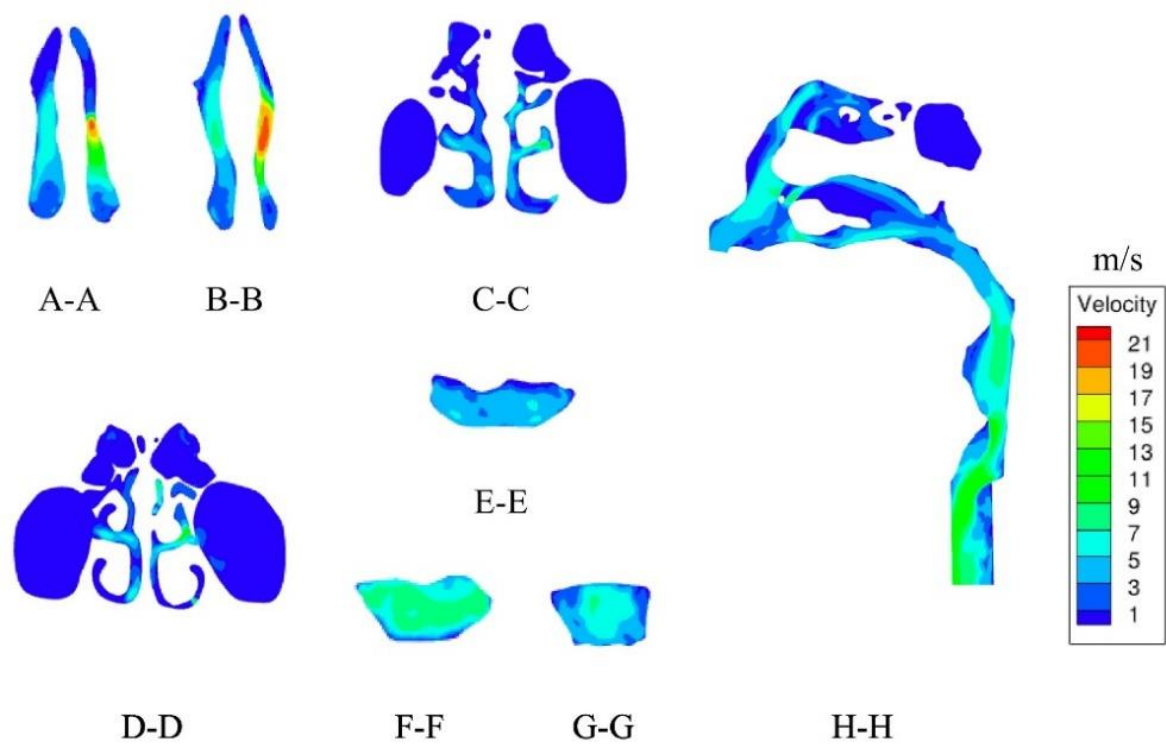


Figure 8: Realistic model of URT with cross sections by Liu et al. (2022) [41].



a) $Q_1=15\text{L/min}$



b) $Q_2=30\text{L/min}$

Figure 9: Velocity distribution in different cross-sections by Liu et al. (2022) [41].

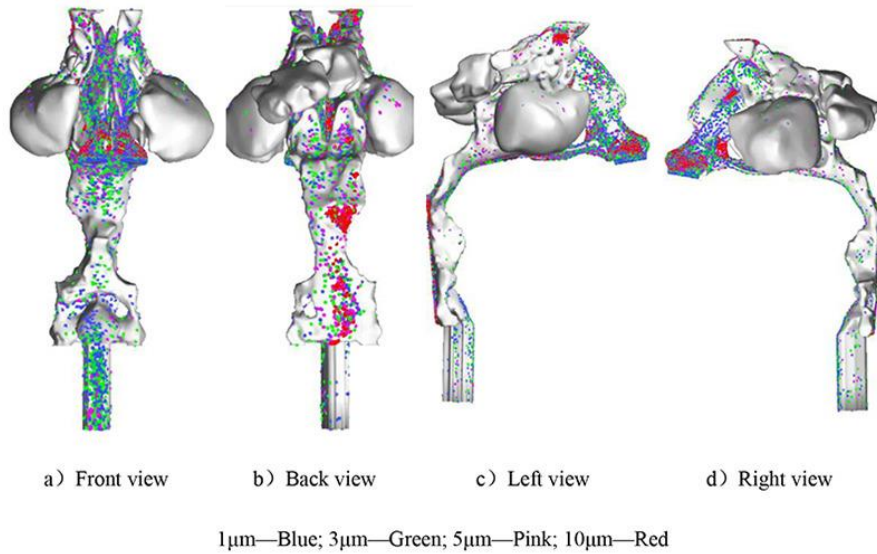


Figure 10: Distribution map of different particle sizes by Liu et al. (2022) [41].

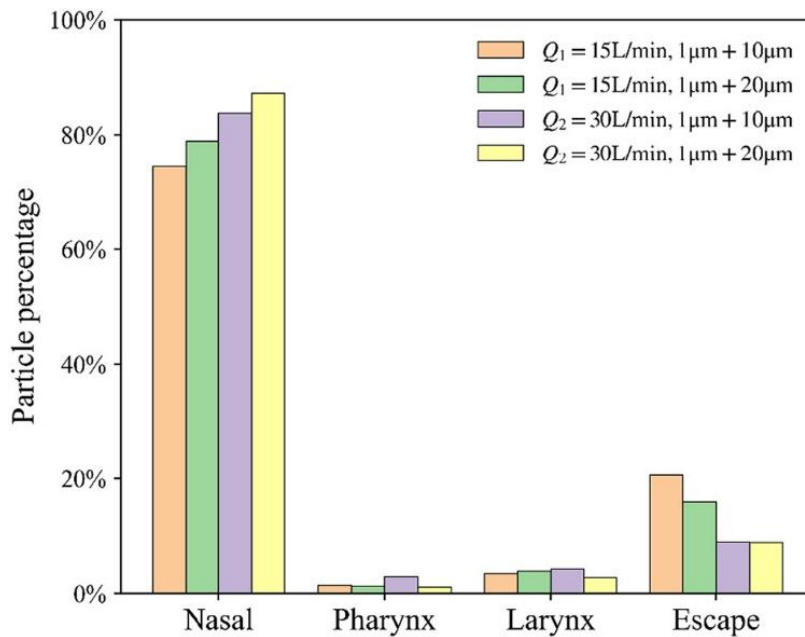


Figure 11: Particle distribution for different sizes by Liu et al. (2022) [41].

To evaluate URT during sneezing **Rahiminejad and his team (2016)** have used realistic URT model consisting of oral and nasal cavity to simulate airflow and pressure field under various sneezing conditions. The k-omega turbulence model is adopted under different conditions (case of nose blockage, sneezing while mouth closed). Their main observations are pressure and velocity where maximum velocity reached in URT is up to 123 m/s found in cross section in nasopharynx. Fluid velocity is accelerated at position where narrowing occurs [42].

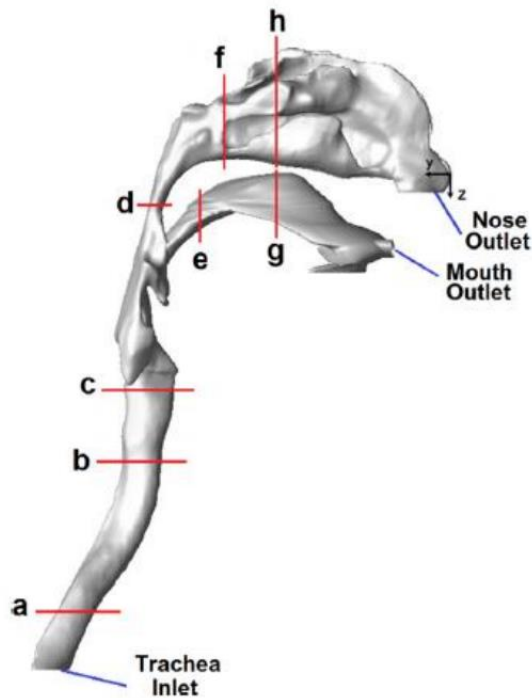


Figure 12: Schematic of geometry utilized by Rahiminejad and his team (2016) [42].

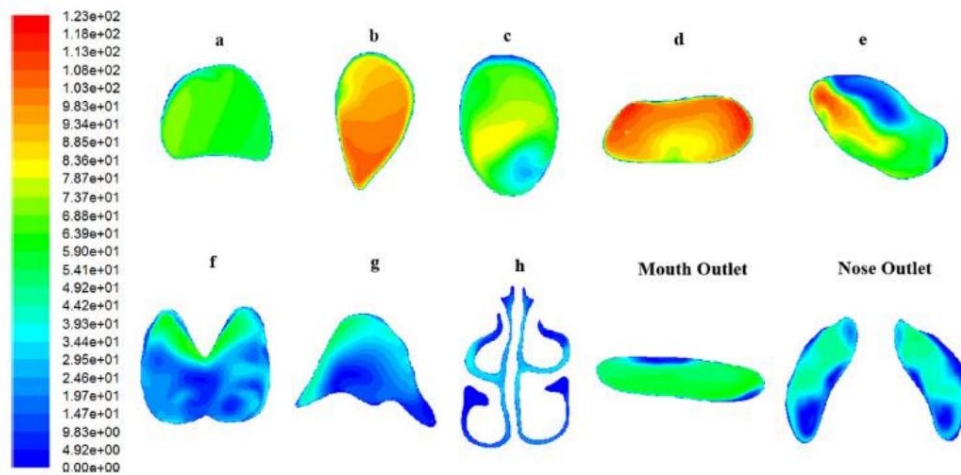


Figure 13: 2D velocity magnitude contours for the flow rate of 470 l/min [42].

Xu and his team (2020) contributed to the research of URT with viscous models exploration. They focused on the trachea region to better understand the glottal jet phenomenon. Different viscous models were compared to understand which one provides the most real-world performance results during inhalation and exhalation. In the contours can be seen how big significance has the viscous model selection on the results. CFD simulation with flow rates of 36 L/min, 64 L/min and 90 L/min. The results form CFD simulations are validated and

compared with the real-world experimental measurement. The RNG $k-\omega$ model and SST $k-\omega$ model were recommended to simulate the flow field in the respiratory tract [39].

Song et al. (2019) give example of CFD utilization in medicine where patients with obstructive sleep apnea hypopnea syndrome (OSAHS) were treated. The patients were scanned with CT before and after application of oral appliances, to evaluate the results of the research. The area 3 (glottis) from Figure 14 was examined if the cross-section became wider. In this study RNG $k-\epsilon$ turbulence model was utilized with flow rate of 12 l/min. The results show significant improvement of flow rate in the glottis area [15].

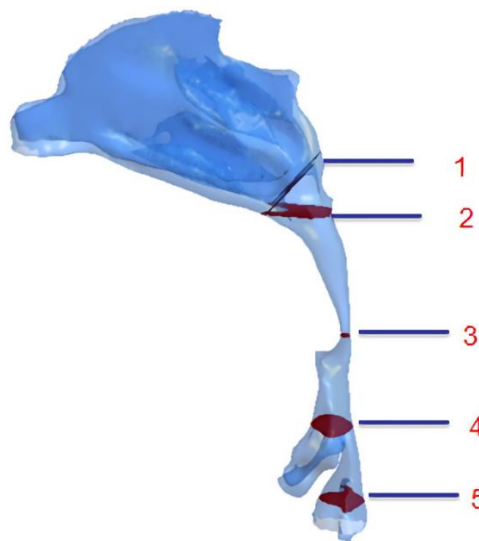


Figure 14: Model preview and Selected sections of the CFD model by Song et al. (2019) [15].

5 Methods

5.1 Model Description

The model was segmented from CT scans in previous work with semi-automatic segmentation combining thresholding and growing seed algorithms. The geometry is based on the CT scans of a 20-year-old male. The selected dataset contained 280 images with a slice thickness of 0.75 mm and was exported in a Digital Imaging and Communications in Medicine (DICOM) format for further processing. The outcomes of the semiautomatic segmentation were inspected on a slide-by-slide basis, and the segmentation parameters were adapted to obtain a precise segmentation of the upper airways. The resulting 3D model was exported as a Standard Triangle Language (STL) [7]. The geometry used for final CFD investigation is shown in Figure 15. The model contains topological data of realistic URT. It has 2 nasal inlets, mouth inlet and trachea outlet.

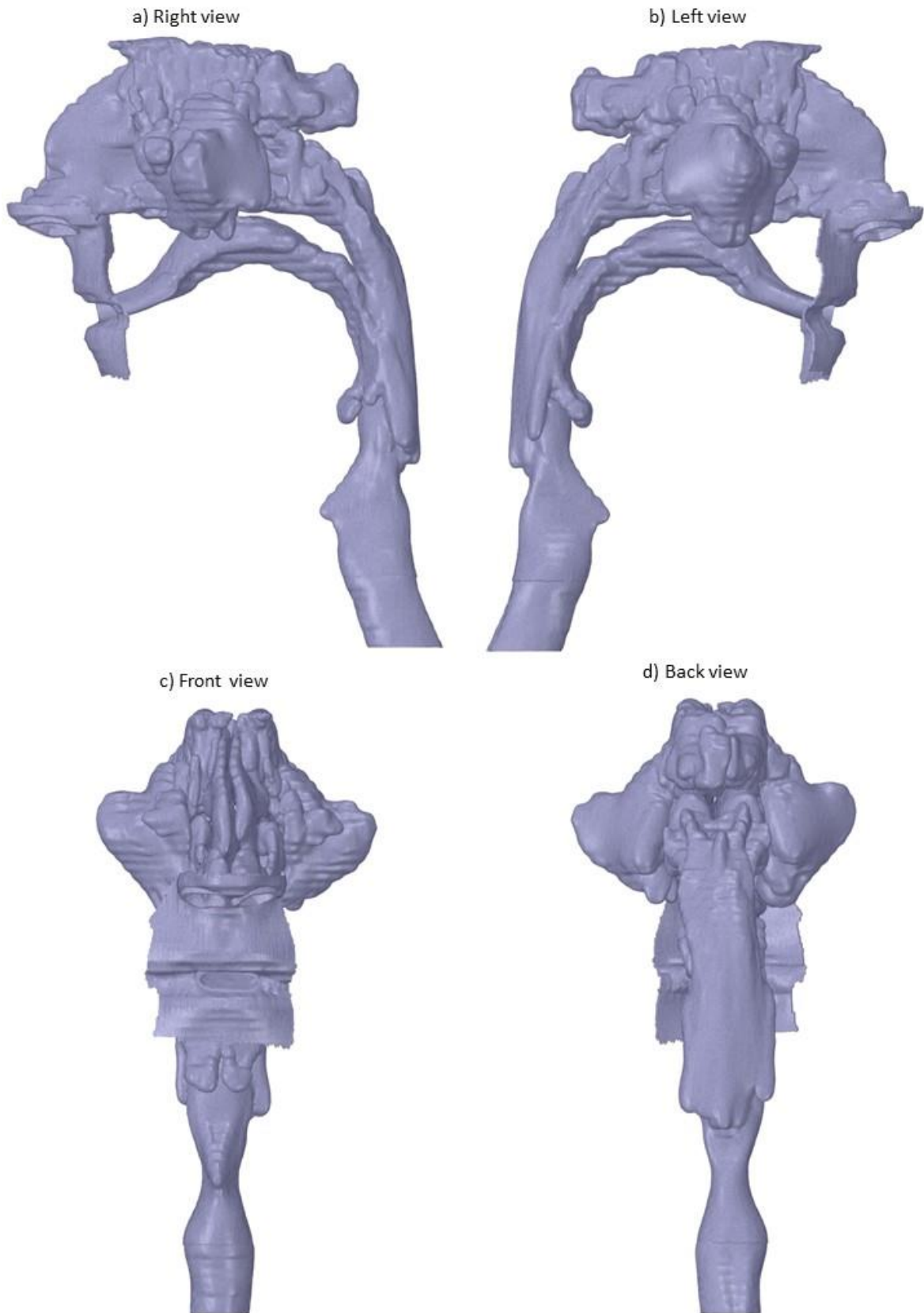


Figure 15: Model preview from four different sides.

5.2 LES Governing Equations

Currently LES is the most viable and promising numerical tool for simulating realistic laminar-transitional-turbulent flows. In LES the large-scale motions (large eddies) of turbulent flow are computed directly and small-scale motions are modelled. In our case we are using low-pass filter, resulting in a significant reduction in computational cost compared to DNS [38].

In LES only large eddies (large scale fluctuations) are calculated. Low-pass filter is applied to the motion of fluid which in the turbulent flow creates smaller and smaller vortices (also called scales). This simplification significantly reduces the computational complexity with preserving enough essential information. This is called explicit filtering. In Figure 16 notice the difference between the filtered velocity \bar{u}_i and the instantaneous velocity u_x [38].

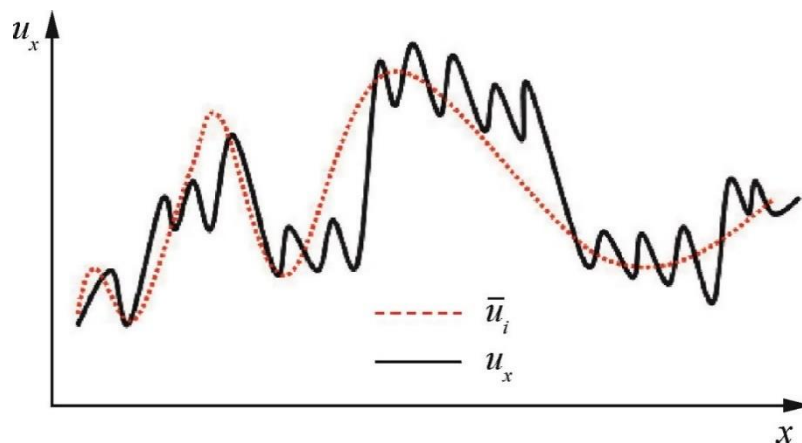


Figure 16: Difference between the filtered velocity \bar{u}_i and the instantaneous velocity u_x [38].

Fluent solves four sets of equations. The momentum equations and the continuity equation govern the mean flow quantities; turbulence modeling equations govern the flow turbulence; and the Discrete Phase Model (DPM) solves for the particle motion. To develop a mathematical model of fluid motion, it is first necessary to start with the Lagrangian form of the equations (differential), which are the basic formulation of physical laws. However, they are not convenient for the formulation of CFD governing equations. Therefore, these equations are transformed into Eulerian form (algebraic) with the help of the Reynolds Transport Theorem [43].

5.2.1 Conservation of Mass

Also known as continuity equation states that mass cannot either be created or destroyed. This means that liquid that enters the system will also come out of the system. Note that for the compressible fluids it is possible to increase or decrease the mass in a fixed volume system. But we consider fluid to be incompressible [34], [43] according to

$$\frac{\partial M}{\partial t} = \frac{d}{dt} \iiint_{\Omega} \rho \, d\Omega = 0 \quad (1)$$

where M is mass, t is time, Ω is volume of fluid parcel, ρ is density.

With use of Reynolds Transport Theorem, we transform the equation into Eulerian form

$$\iiint_{\Omega} \frac{\partial \rho}{\partial t} \, d\Omega + \oint_A \rho \vec{v} \cdot \hat{n} \, dA = 0 \quad (2)$$

\hat{n} is normal vector, A is surface area of fluid parcel [34], [43].

Then we apply the divergence theorem to substitute the surface integral into volume integral

$$\iiint_{\Omega} \left(\frac{\partial \rho}{\partial t} + \nabla \cdot \rho \vec{v} \right) d\Omega = 0 \quad (3)$$

Since the integral is satisfied for arbitrary volume, the expression can be written as

$$\frac{\partial \rho}{\partial t} + \nabla \cdot \rho \vec{v} = 0 \quad (4)$$

Which is the commonly used continuity equation for the compressible flow of a fluid with density ρ and velocity \vec{v} [34], [43].

This equation can be expressed in Cartesian form if we substitute the divergence term, we get expression for 3D

$$\frac{\partial \rho}{\partial t} + \frac{\partial(\rho u)}{\partial x} + \frac{\partial(\rho v)}{\partial y} + \frac{\partial(\rho w)}{\partial z} = 0 \quad (5)$$

Or expression for 2D after removing the component in z direction

$$\frac{\partial \rho}{\partial t} + \frac{\partial(\rho u)}{\partial x} + \frac{\partial(\rho v)}{\partial y} = 0 \quad (6)$$

For incompressible fluids where volume doesn't change, the density is assumed to be constant which will simplify the continuity equation to following form (telling us that divergence of velocity is equal to zero) [34], [43]

$$\nabla \cdot \vec{v} = 0 \quad (7)$$

In Cartesian notation is as follows

$$\frac{\partial u}{\partial x} + \frac{\partial v}{\partial y} + \frac{\partial w}{\partial z} = 0 \quad (8)$$

5.2.2 Conservation of Momentum

This equation is based on the Newton's second law.

$$\frac{d(M\vec{v})}{dt} = \frac{d}{dt} \iiint_{\Omega} \rho \vec{v} d\Omega = \vec{F}_s + \vec{F}_b \quad (9)$$

This expression states that the rate of change of momentum of fluid particle equals to the sum of forces acting on the particle. Time derivative represents the time rate of change of the fluid momentum. Surface forces \vec{F}_s (pressure and friction) and body forces \vec{F}_b (gravity) acting on the fluid [34], [43].

We can use Reynolds Transport Theorem, to transform the equation into Eulerian form

$$\iiint_{\Omega} \frac{\partial(\rho\vec{v})}{\partial t} d\Omega + \iint_A \vec{v}(\rho\vec{v} \cdot \hat{n})dA = \vec{F}_s + \vec{F}_b \quad (10)$$

Then with divergence theorem we can substitute the surface integral into volume integral

$$\iiint_{\Omega} \left(\frac{\partial(\rho\vec{v})}{\partial t} + \vec{v} \nabla \cdot (\rho\vec{v}) \right) d\Omega = \vec{F}_s + \vec{F}_b \quad (11)$$

The \vec{F}_s term on the right side of the equation refers to surface forces acting on the fluid particle due to pressure and viscous stress [34], [43].

$$\vec{F}_s = \vec{F}_p + \vec{F}_v \quad (12)$$

where these forces can be further written as

$$\vec{F}_p = - \iint_A p \hat{n} dA \quad (13)$$

$$\vec{F}_v = \iint_A \bar{\tau} \cdot \hat{n} dA \quad (14)$$

where $\bar{\tau}$ is viscous stress tensor [34], [43].

With divergence theorem we can transform these two equations into volume integral form and we obtain

$$\vec{F}_p = - \iiint_{\Omega} \nabla p \, d\Omega \quad (15)$$

$$\vec{F}_v = \iiint_{\Omega} \nabla \cdot \bar{\tau} \, d\Omega \quad (16)$$

\vec{F}_b refers to the gravitational force

$$\vec{F}_b = \iiint_{\Omega} \rho \vec{g} \, d\Omega \quad (17)$$

If we substitute these expressions, we just derived to the volume equation we obtain

$$\iiint_{\Omega} \left(\frac{\partial(\rho \vec{v})}{\partial t} + \vec{v} \cdot \nabla (\rho \vec{v}) \right) d\Omega = \iiint_{\Omega} (-\nabla p + \nabla \cdot \bar{\tau} + \rho \vec{g}) \, d\Omega \quad (18)$$

If we assume the control volume is arbitrary hence the integrals are equal to zero to satisfy the conservation equation [34], [43]. The equation is then reduced to its differential form

$$\rho \left(\frac{\partial \vec{v}}{\partial t} + \vec{v} \cdot \nabla \vec{v} \right) = -\nabla p + \nabla \cdot \bar{\tau} + \rho \vec{g} \quad (19)$$

where ρ is density of the fluid, $\frac{\partial \vec{v}}{\partial t}$ represents velocity change in time, $\vec{v} \cdot \nabla \vec{v}$ is speed and direction of the fluid, ∇p is pressure gradient, $\nabla \cdot \bar{\tau}$ is internal forces of viscosity, $\rho \vec{g}$ is external forces of gravity

$\bar{\tau}$ is viscous stress tensor, 3 by 3 matrix which gives us nine unknowns. In this case we would need nine additional equations to close the problem. To reduce complexity and computational time we can utilize approach introduced by Navier, which was then refined by Stokes, and express the viscous stress tensor in terms of flow variables which will leave us with one equation [34], [43].

$$\bar{\tau}_{ij} = 2\mu \left(\varepsilon_{ij} - \frac{1}{3} \nabla \cdot \vec{v} \delta_{ij} \right) \quad (20)$$

where μ is the dynamic viscosity, ε is the strain rate tensor, δ is referred to as Kronecker delta [34], [43].

To obtain equation (20), these fundamental assumptions must be complied: 1. No viscous stresses are generated by pure translation and body rotation. 2. The fluid must be isotropic – the properties are same in every direction. 3. And the fluid has to be Newtonian. 4. The last assumption is, that the stress force should act only tangentially [34], [43].

After substitution to conservation of momentum equation we get

$$\rho \left(\frac{\partial \vec{v}}{\partial t} + \vec{v} \cdot \nabla \vec{v} \right) = -\nabla p + \mu \nabla^2 \vec{v} + \frac{1}{3} \mu \nabla (\nabla \cdot \vec{v}) + \rho \vec{g} \quad (21)$$

This equation is typically referred as convective form of momentum equation.

This equation can be written in Cartesian coordinates after which this equation will further expand into 3 equations in x, y and z direction. Conservative form for conservation of momentum equation is

$$\frac{\partial(\rho u)}{\partial t} + \nabla \cdot (\rho \vec{v} u) = -\frac{\partial p}{\partial x} + \nabla \cdot \left(\left(\frac{\partial \vec{v}}{\partial x} + \nabla u \right) - \frac{2}{3} \mu (\nabla \cdot \vec{v}) \hat{i} \right) + F_{b,x} \quad (22)$$

$$\frac{\partial(\rho v)}{\partial t} + \nabla \cdot (\rho \vec{v} v) = -\frac{\partial p}{\partial y} + \nabla \cdot \left(\left(\frac{\partial \vec{v}}{\partial y} + \nabla v \right) - \frac{2}{3} \mu (\nabla \cdot \vec{v}) \hat{j} \right) + F_{b,y} \quad (23)$$

$$\frac{\partial(\rho w)}{\partial t} + \nabla \cdot (\rho \vec{v} w) = -\frac{\partial p}{\partial z} + \nabla \cdot \left(\left(\frac{\partial \vec{v}}{\partial z} + \nabla w \right) - \frac{2}{3} \mu (\nabla \cdot \vec{v}) \hat{k} \right) + F_{b,z} \quad (24)$$

And is generally applied for CFD modeling [34], [43].

So far, we have 4 unknowns (u, v, w, p) and 4 equations (momentum-x, momentum-y, momentum-z, and continuity equation) so we can resolve the mathematical model. If we were dealing with compressible fluid, we would need to add conservation of energy equation.

5.2.3 Conservation Energy

Conservation energy is based on the first law of thermodynamics. For this case where compressibility and heat transfer are not considered the fluid is assumed isothermal and thus the equation is not required.

5.2.4 Discrete Phase Model for Particle Deposition

Discrete phase model (DPM) determines particle deposition by tracking individual particles as they move through the flow field using a Lagrangian approach. Particles tracked by this equation are inert and exert no influence over the flow solution. Conditions must exist at each boundary to apply this equation.

Unsteady particle tracking is enabled – each particle is advanced by a specified number of particle time steps, unlike steady particle tracking, we are interested in progression of the particle in time. Unsteady tracking is used to see particle deposition in time. Steady shows the results where the solution reaches its final convergence.

Particles are considered to be spherical. One-way coupling between the flow and the particles is assumed, which means that the flow affects the particles, but the effect of particles on the flow is negligible [44]. Particles are also assumed to be dilute in the continuous phase and do not interact.

Particle trajectory is predicted by integrating the force balance on the particle, written in Lagrangian reference frame [45].

$$\frac{du_p}{dt} = F_D(u - u_p) + \frac{g_z(\rho_p - \rho)}{\rho_p} + F_x \quad (25)$$

where u_p is initial particle velocity, u is fluid phase velocity, ρ_p is the density of particle, ρ is the fluid density, g_z is the gravitational force in z direction. F_x is additional acceleration term, F_D represents drag force according to

$$F_D = \frac{18\mu C_D Re}{\rho_p d_p^2 24} \quad (26)$$

Where μ is molecular viscosity of the fluid, d_p is particle diameter, Re is Reynolds number which is defined as

$$Re = \frac{\rho d_p |u_p - u|}{\mu} \quad (27)$$

5.3 Meshing

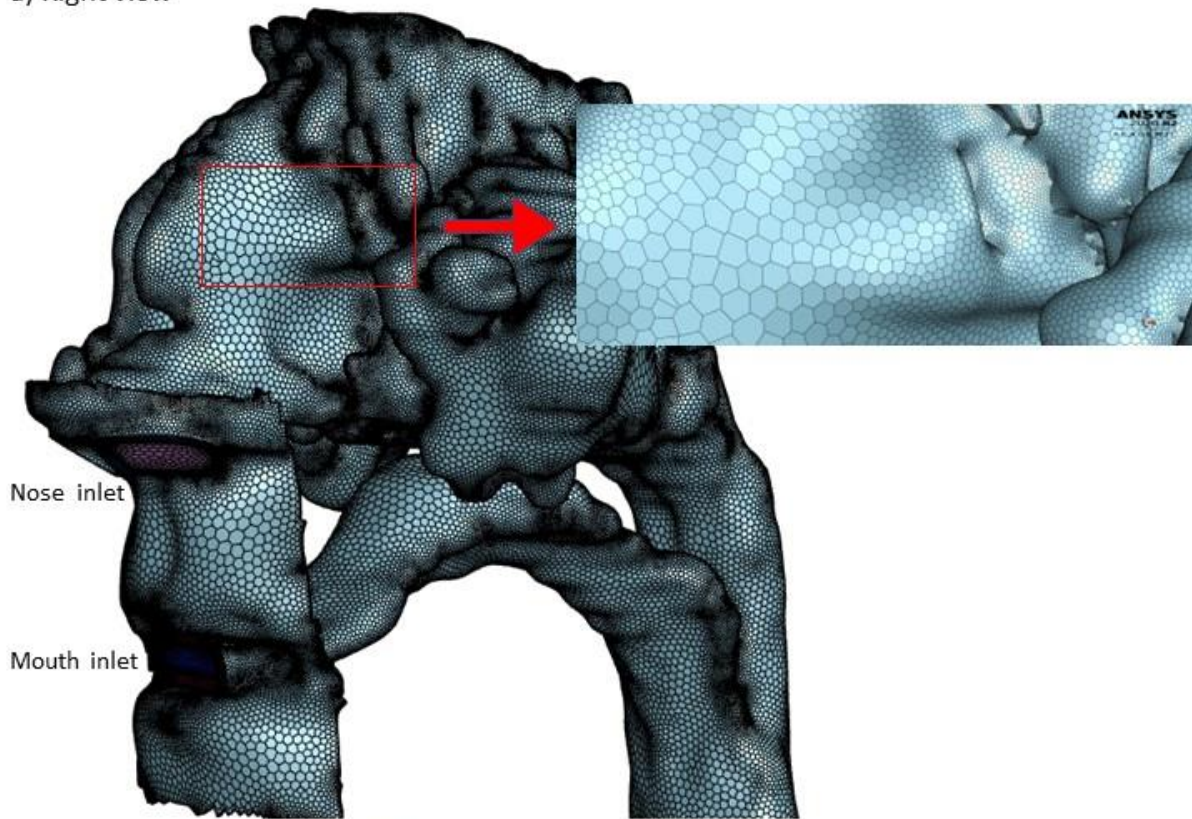
The primary and critical step in numerical modelling is the computational domain discretization. This step is called meshing. Generally, the geometry used for simulations is too complex and we can't compute the Navier–Stokes equation for this problem. We need to divide the model into smaller parts called elements or cells, where the equations can be solved. In 3D, these elements have usually tetrahedron, hexahedron or polyhedron shape. The more cells the mesh has, the better the simulation is. But we must keep in mind that the finer the mesh is, the more computationally demanding the solution is.

To generate mesh, ANSYS (2020) – Fluent with meshing, was utilized. Unstructured mesh was generated. Hexahedral and polyhedral elements were used to create mesh. Combination of these two meshing elements is called poly-hexcore. This mesh starts with polyhedron cells and the mesh in core is hexahedral. To obtain efficient results for the near-wall effects, three inflation layers were implemented in the flow region adjacent to the solid body. Solid body is meshed with just polyhedron elements (see Figure 17).

To achieve very accurate results in CFD, it is recommended to divide the flow domain into hexahedral elements [46]. Hexahedral elements are characterized with accurate results. However, this element type is not always applicable for more complex geometry. In these domains, the polyhedral elements are preferable for use. The major benefit of polyhedral elements is that each individual cell has many neighbors, so gradients can be much better approximated in comparison to tetrahedron elements [46].

Grid sensitivity study was performed to assess the grid independency of the computed results. The mesh, consisting of 3 426 832 cells, that is used for the simulations, showed mild discrepancy in the flow pattern in some regions, but produced almost the same results as a finer mesh consisting of 6 325 963 cells. A coarser mesh consisting of 1 563 896 cells was not able to reproduce the results because it did not have the required resolution.

a) Right view



b) Longitudinal cross section

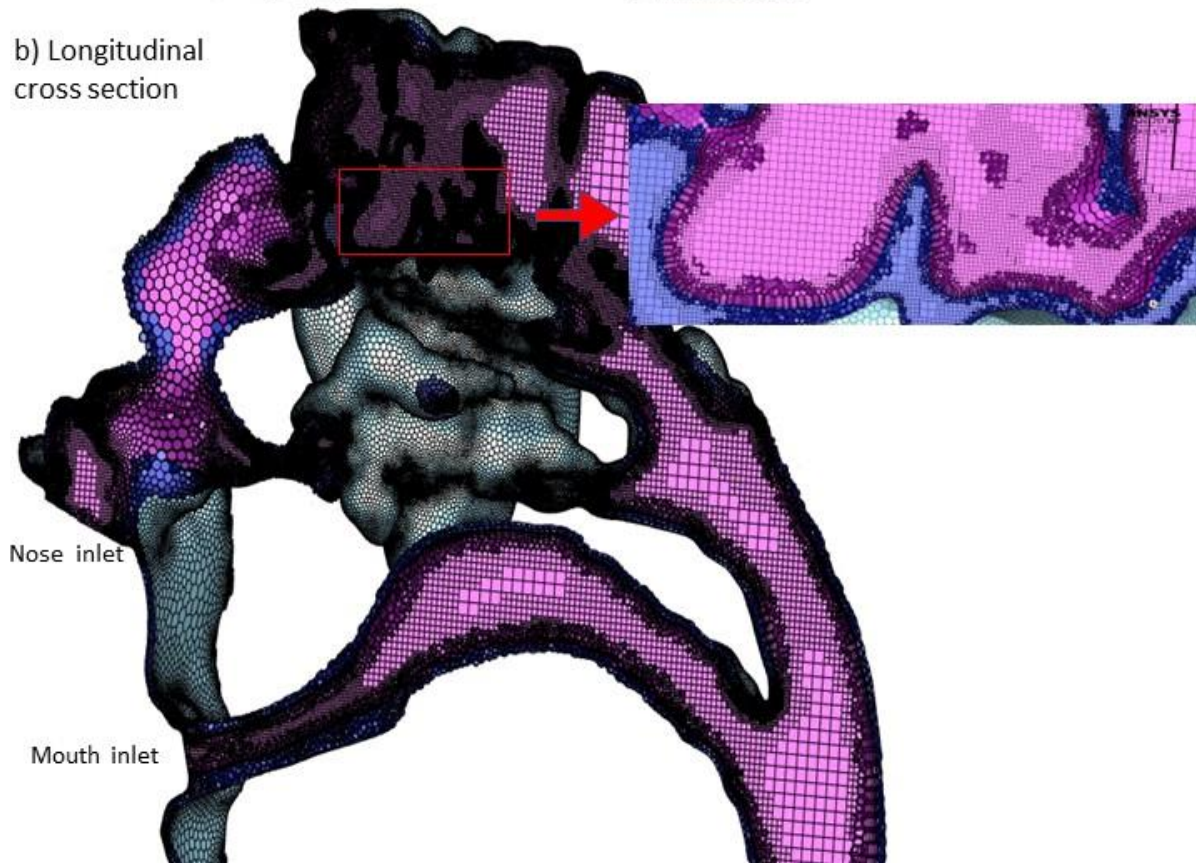


Figure 17: 3D mesh model of the upper airways with poly-hexcore unstructured mesh.

5.4 Boundary Conditions and Initialization

Prior to the computational process, boundary conditions and initial conditions need to be specified. Boundary conditions designate what happens at the edges of the flow domain and thus are necessary for solving the flow field. The boundaries for this problem include the mouth and nose inlet, the trachea outlet, and the wall. An initial condition represents the fluid state before the first step.

Fluent setting that was used for the CFD simulation in this thesis, is described in Table 1.

Air within the human respiratory tract is considered homogeneous, Newtonian, and incompressible. The outlet boundaries were defined to be pressure outlets of zero-gauge pressure. Double precision solver was selected at the initial launching window of Fluent. Second order upwind schemes were used for momentum and turbulent kinetic energy and specific dissipation rate. The convergence criteria were set to be 10^{-3} . Pressure based solver is chosen.

In DPM settings, the escape boundary condition type is applied to both inlet and outlet. A user-defined function is applied to wall to obtain a graphical visualization of particle deposition in the model. This user-defined function simulates a trap condition, meaning any particle that touches the wall is considered to be trapped at that location. Assuming the walls of the respiratory tract are coated in mucous and saliva, which is sticky, thus particles colliding with the wall will not be able to detach.

Initial velocity of particles is set to be the same as inlet flow rate. Several different sizes of particles are adopted, to observe the deposition rate effect in terms of particle size. Specific number of particles are injected through the inlet in normal direction from the inlet surface. During nasal inhalation, there was 14 860 particles. During oral inhalation, 4 560 particles. Only inhalation is simulated in this work.

The calculation time depends mainly on the time steps selected at the beginning of the Fluent settings. If big time step is selected, the calculation takes shorter time, but we don't see the particle movement in time. Furthermore, for the sake of precision it is recommended to select shorter time step. The compromise needs to be found.

The duration of nasal inhalation is two seconds, and during the oral inhalation, one second. The time step selected in this work is 0,02 seconds and is performed a hundred times. This makes the total of two seconds in nasal inhalation. During oral inhalation, the time step is 0,02 seconds and is calculated fifty times.

Table 1: Fluent setting used during computation

General:	
Type	Pressure-based
Velocity formulation	Absolute
Time setting	Transient
Gravity	$g = -9.81$ in Z-direction
Models:	
Viscous	LES Smagorinsky-Lilly
DPM setup	Disabled Interaction with continuous phase (valid only for 2-way coupling) Unsteady Particle Tracking Max Number of steps: 50,000 Step length factor: 5
Injection	Material: Calcium Carbonate with density of 1425 kg/m^3 Particle type: inert Injection type: surface – inlet Velocity: in face normal direction, same as flow rate Diameter distribution: Rosin-Rammler Diameter: $1\text{-}10\mu\text{m}$ Total flow rate: $1\text{e-}10 \text{ kg/s}$ Time: 0-0s
Initial and boundary conditions	Inlet: velocity inlet, $2,01\text{m/s}$ $4,1\text{m/s}$ $27,1\text{m/s}$ DPM – escape Turbulence intensity 5%, Turbulent viscosity ratio of 10 Outlet: pressure outlet, gauge pressure 0, DPM-escape Wall: No-slip, Material – PLA, DPM – UDF
Solution → methods:	
Scheme	SIMPLE
Gradient	Least Squares Cell Based
Pressure	Second-Order
Momentum	Bounded Central Differencing
Transient Formulation	Bounded Second Order Implicit
Monitors → Residuals	Absolute criteria 10^{-3}
Initialization	Hybrid
Run calculation	Number of time steps – 100 Max iteration/time step – 400 Time step size – 0.02

6 Results

Airflow contours, like velocity and pressure, are displayed in this chapter along with particle deposition under various flow rates. In this work flow rates of 15 l/min, 30 l/min and 90 l/min are used. The results should help us understand the flow phenomena and deposition of medicaments in URT. Two different types of inhalations are simulated. First, inhalation through nose simulating the inhalation with nebulizer with airflow rates of 15 l/min and 30 l/min. Second, through mouth simulating inhalation with dry-powder inhaler with flow rate of 90 l/min.

Following cross sections displayed in Figure 18 were used to better understand what is happening inside the model, and to display the results.

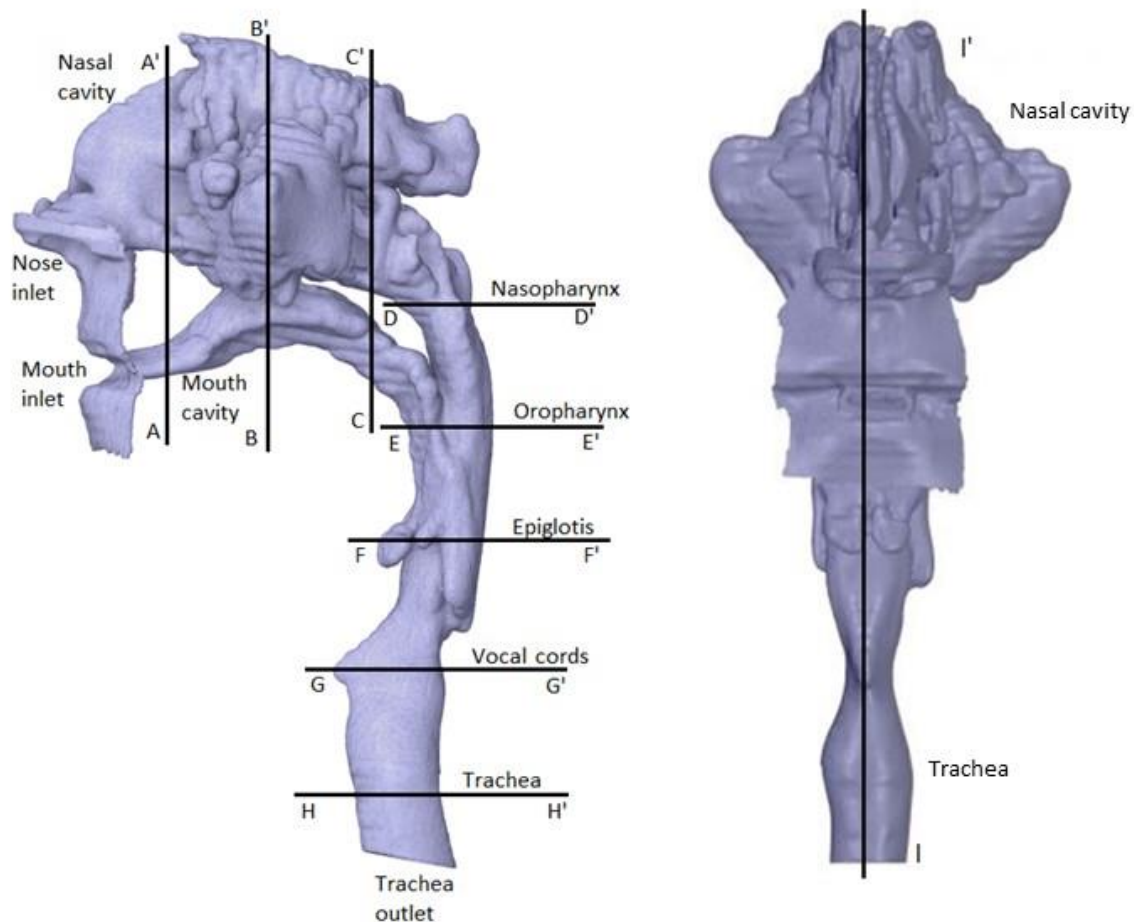


Figure 18: Cross sections in transverse and longitudinal direction

6.1.1 Velocity Contours

Figure 19 shows the series of velocity contours in cross sections displayed in Figure 18. Inhaled air divides naturally between the right and left nostrils. We can see rapid increase in velocity (6,3 m/s) in right nostril in A-A' section due to narrowing of the pathway. Due to differences in the structure of the left and right nasal passages, the velocities are different. It is a common phenomenon that one nostril has a higher velocity than the other. It is due to the different blood supply in the nasal cavity. The velocities in the left and right nostril can change throughout life. The air then gradually flows into the paranasal sinuses.

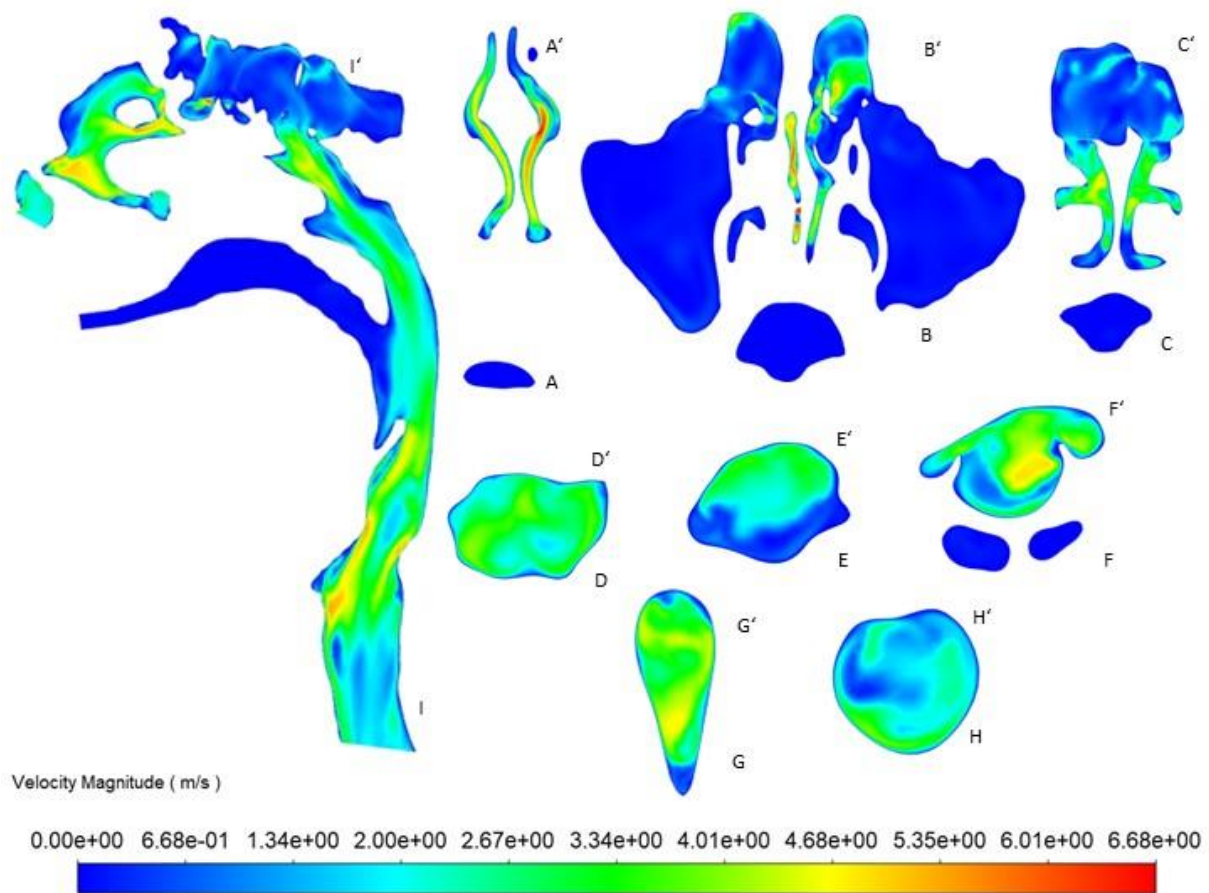


Figure 19: Velocity contours with flow rate of 15 l/min.

When the air flows to the nasal cavity outlet (section C), the confluence of the flow from paranasal sinuses causes uneven velocity distribution in this area. This is manifested in the vortices in the whole section. In the I-I' cross section, we can observe a gradual decrease in velocity from the nostrils up to the oropharynx and significant increases in the narrowing near to epiglottis and vocal cords. Followed again by the drop in velocity. In the pharynx and larynx, the maximum airflow velocity appears near the back wall surface. While near the exit, the larger airflow velocity appears near the front wall surface. During inspiration, the velocity increases from near 3,14 m/s at the nostrils to the maximum value of 6,68 m/s in the nasal cavity due to its narrowing. Distribution of velocity in each cross section is not homogeneous

due to high Reynolds number and turbulent vortices. This results in velocity fluctuations. This is due to the complex structure of the nasal cavity and the disturbances arising from the convergence of airflows. Flow in the supraglottic region is dominated by the so-called laryngeal jet, issuing from the constrictions through the epiglottis and the back of the tongue. Here, we can observe an increase in velocity from section F all the way up to G. Behind the epiglottis, the velocity decreases again.

In Figure 20 when the inspiratory flow increases to 30 l/min, the change of maximum air velocity is obvious in the whole URT. We can notice that maximum velocity in the URT has risen from 6,68 m/s to 13,5 m/s. Though, when compared with Figure 19, the contours are not very different from each other. Again, its maximum can be found in the section A-A'. Generally, the same structure of the flow can be observed for both flow rates (15 l/min and 30 l/min). The main difference is in the strength of the flow that is visible in the longitudinal cross section I-I'. The increased inspiratory flow results also in a more unevenly distributed velocity. The turbulent vortices are more obvious.

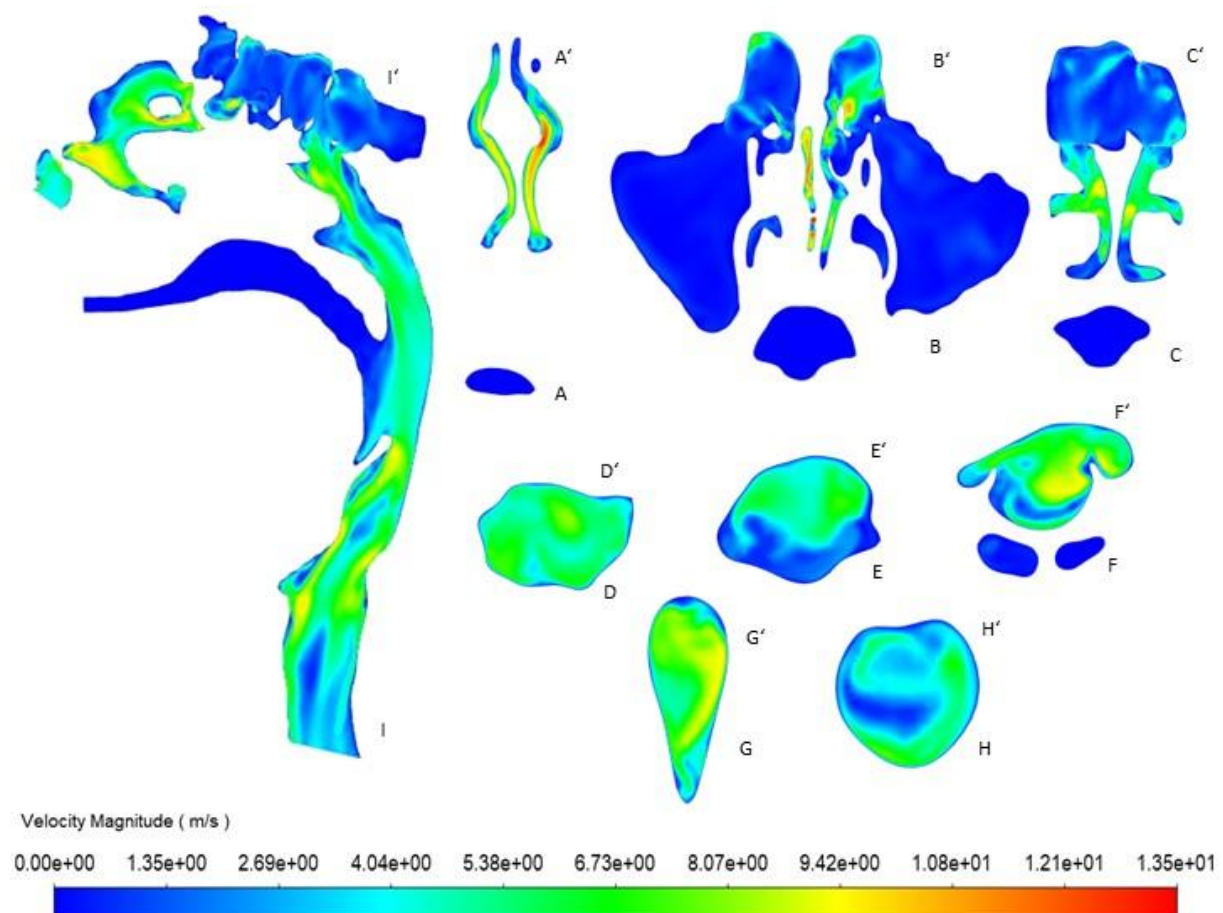


Figure 20: Velocity contours with flow rate of 30 l/min.

Figure 21 represents oral inhalation (with Dry powder inhaler). The flow rate through mouth is 90 l/min and flow rate at the beginning of nasal cavity is set to 30 l/min.

During the main inspiration through mouth with flow rate 90 l/min we can see the highest velocity is at the entrance of the oral cavity. The velocity is rapidly decreased in the oral section C-C' where the flow collides with the soft palate. Gradual increase in velocity can be seen again in section F up to G (epiglottis – vocal cords).

Near the walls we can see typical velocity stagnation. This phenomenon occurred in all inspiratory flow rates but is less significant with higher flow rates in regions where high turbulent kinetic energy is present.

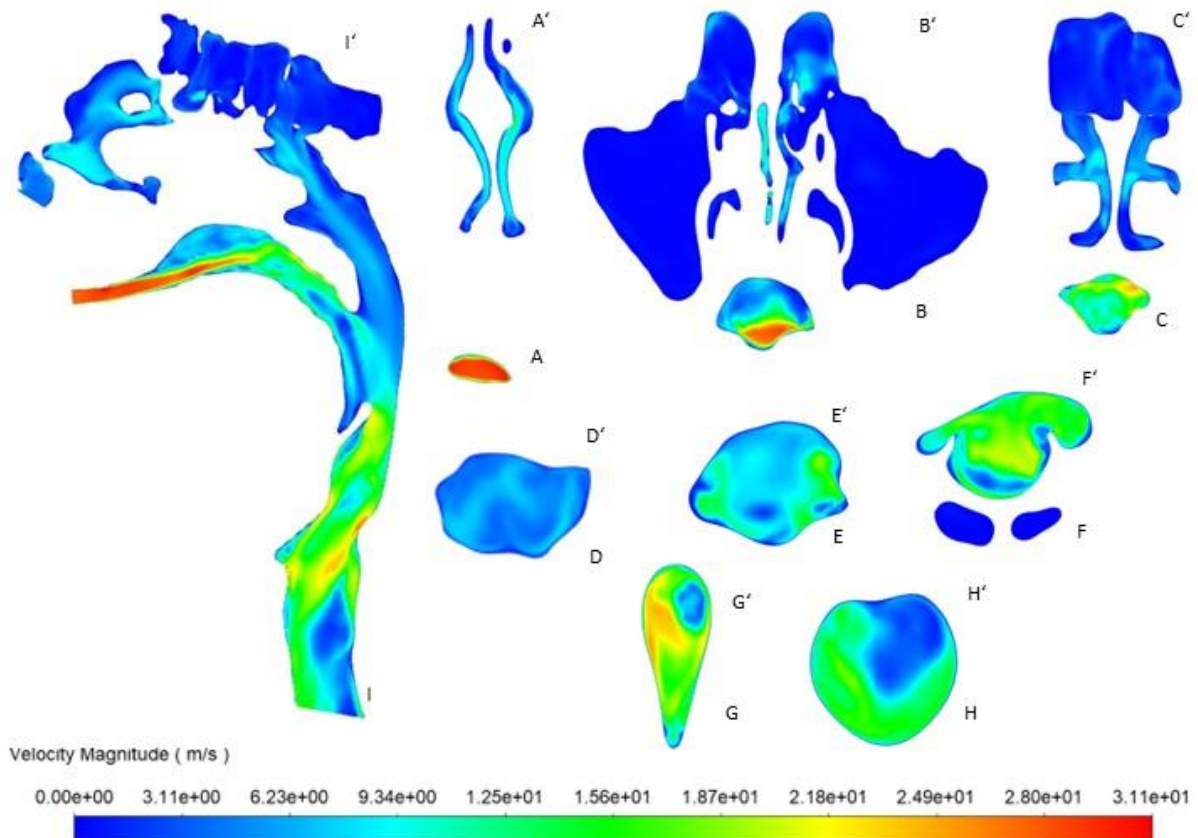


Figure 21: Velocity contours with flow rate of 90 l/min.

6.1.2 Pressure Contours

During nasal inspiration with flow rate of 15 l/min (Figure 22), pressure falls rapidly from the nares as it goes deeper into upper respiratory tract. We can notice the scale ranges from 101 319 Pa to 101 390 Pa. There is almost 70 Pa difference from the start of the nose and in the end of trachea.

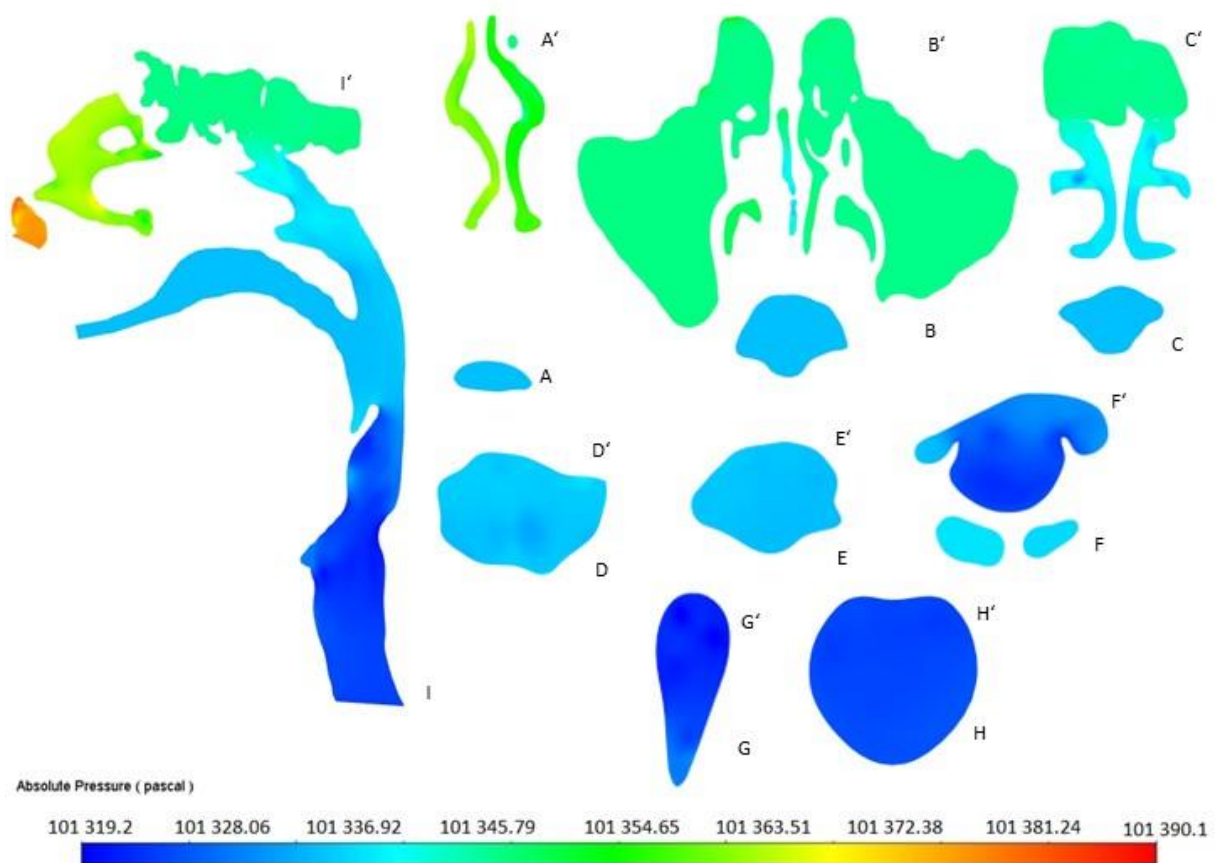


Figure 22: Pressure contours with flow rate of 15 l/min.

The pressure in the oropharynx and laryngopharynx is relatively constant, followed by a further pressure drop as flow accelerates in the epiglottis area and further stays low in the trachea region. A pressure minimum occurs in the narrowest region of the epiglottis and vocal cords. This is because when velocity rapidly expands, the pressure on the other hand rapidly drops. The absolute pressure then stays decreased up to end of the trachea.

We can notice vortices in the C section. This is due to the complex structure of the nasal cavity and the disturbances arising from the convergence of airflows.

The laryngeal jet is the most important flow feature occurring in the throat during rapid inhalation. This phenomenon determines mean and fluctuating behavior of the flow downstream in the tracheobronchial airways.

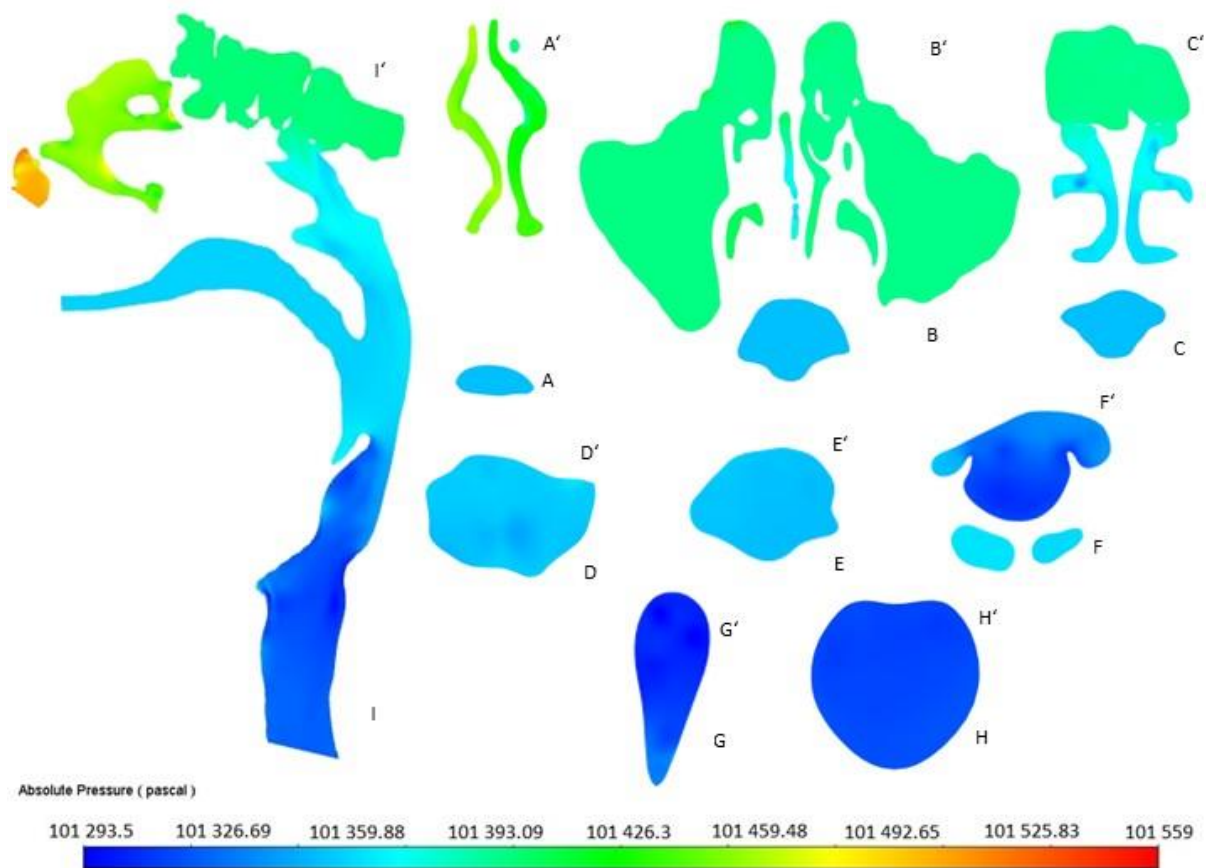


Figure 23: Pressure contours with flow rate of 30 l/min.

Figure 23 is representing inhalation through nose with flow rate of 30 l/min. At first glance we can see contours hasn't change much. Though more stream vortices can be clearly seen in the I-I' longitudinal cross section. Also, the overall absolute pressure has changed with the range of 101 293 Pa minimum to maximum of 101 559 Pa which makes the difference of 266 Pa.

Again, there is different pressure between the left and right nostril. Which is due to different anatomical and physiological structure. And we can also notice homogeneous in distribution of pressure in nasal cavity without any fluctuations.

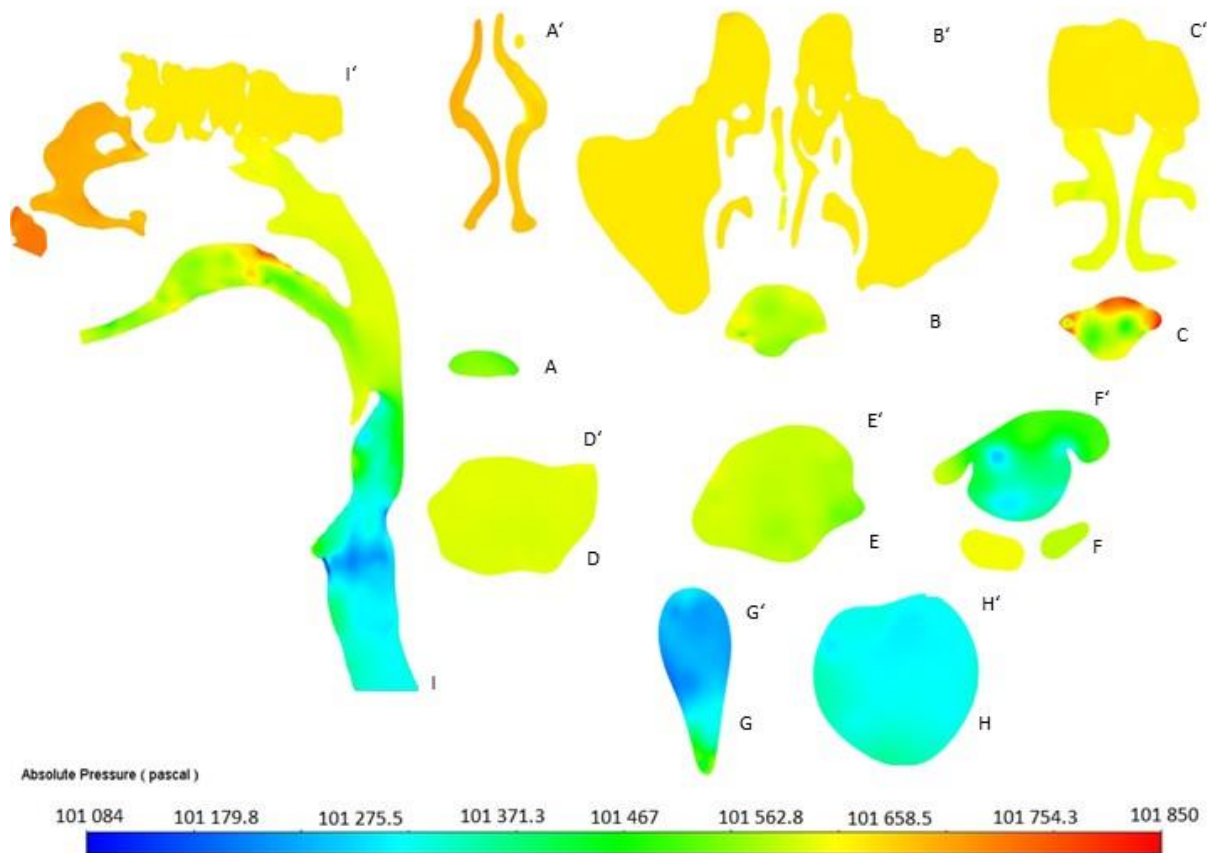


Figure 24: Pressure contours with flow rate of 90 l/min.

With oral inhalation with flow rate of 90 l/min (Figure 24) typical laryngeal jet can be observed in the cross-section G. This phenomenon happens due to the quick change in velocity in vocal cords because of narrowing of this anatomical structure. After cross section G pressure slowly increases in the trachea region.

The highest pressure can be seen in cross section C in the oral cavity, where the air first hits the soft palate. The difference between minimum and maximum pressure is 766 Pa. The pressure from the oropharynx to the subglottis dropped almost by 490 Pa

With a higher flow rate, the laryngeal jet has two phases in comparison with the previous flow rates. The first pressure drop can be clearly seen in the epiglottis, followed by the flow vortices, and then another significant pressure drop happens in the glottis region (G), where the minimum pressure can be found.

We can notice the higher flow rate, the higher pressure maximum appears in the extrathoracic airway. Also, the difference between pressure minimum and maximum is growing significantly.

6.1.3 Particle Deposition

14 860 particles of sizes 1 – 10 μm are injected into both nasal inlets using DPM in a Lagrangian frame with stochastic particle tracking. For oral inhalation, 4530 particles are injected into the mouth opening. The number of deposited particles on the wall and the number of escaped particles at the outlet are used to reflect the deposition rate of inhaled particles. The blue dots represent 1 μm particles, the red dots represent 10 μm particles (see Figure 25).

For each inhalation type, 3 computations were performed to evaluate whether particle deposition changes between calculation processes. It was found that the standard deviation accounts for around 8 - 10 %.

In Figure 25, Figure 26 and Figure 27 is obvious that with increasing flow rate, the increase of velocity of particles causes more particles to be deposited in the upper respiratory tract, especially in the beginning of nasal cavity, and fewer particles to escape from the outlet. It is evident that most particles deposit in the nasal or oral cavity and a small percentage of particles deposit in the pharynx or tracheal area.

The proportion of the particles deposited in each area is ranked as follows: nasal cavity>larynx>pharynx. The increase in inspiratory flow also increases the particle deposition number in the nasal cavity but decreases the amount in the pharynx and larynx.

We can also notice that the smaller the particle size is (1 μm and 3 μm), the more are particles dispersed across the entire URT. On the other hand, particles with larger diameter (5 μm and 10 μm) are comparatively more concentrated in mouth or nasal cavity in front of oropharynx area. Particles of 1 μm and 3 μm deposit more at the upper part of the pharyngeal area. The particles of 5 μm , on the other hand, are rarely deposited in these areas, and the particles of 10 μm are almost never deposited.

When we compare different flow rates during nasal inhalation (Figure 25 and Figure 26), we can notice that even big particles appear in the laryngeal section with flowrate 15 l/min whereas with flowrate 30 l/min these particles tend to deposit rather in the nasal cavities. This is also evident in Figure 28. The proportion of particles deposited in the nasal cavity is higher with flow rate of 30 l/min, accounting for 40 – 47 % in the first section and total of 70 – 74 % in the whole nasal cavity as opposed to the flow rate of 15 l/min, where in the first section A deposited 33 – 40 % of particles and 56 -61 % in the whole nasal cavity.

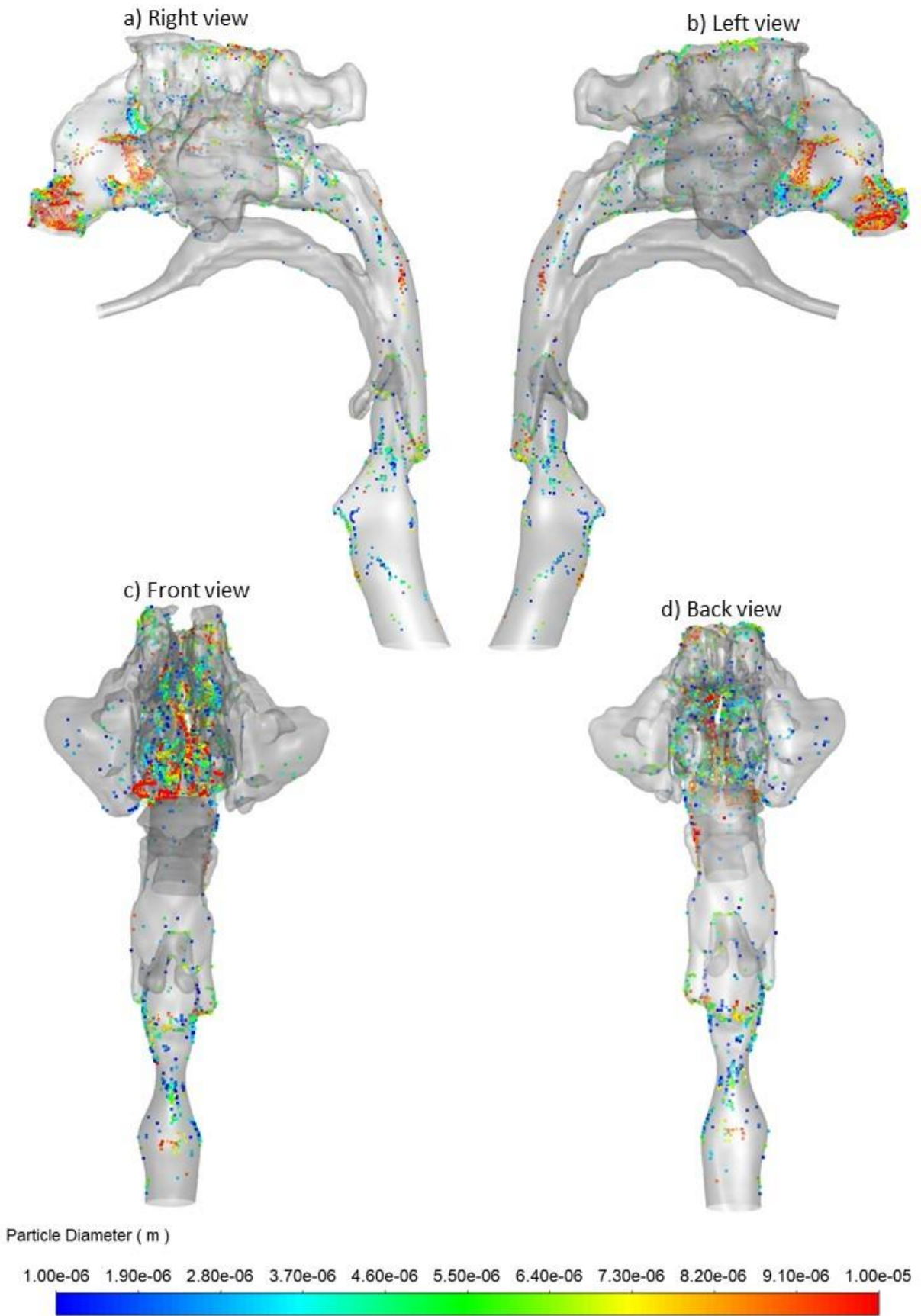


Figure 25: Particle deposition after nasal inhalation with 15 l/min.

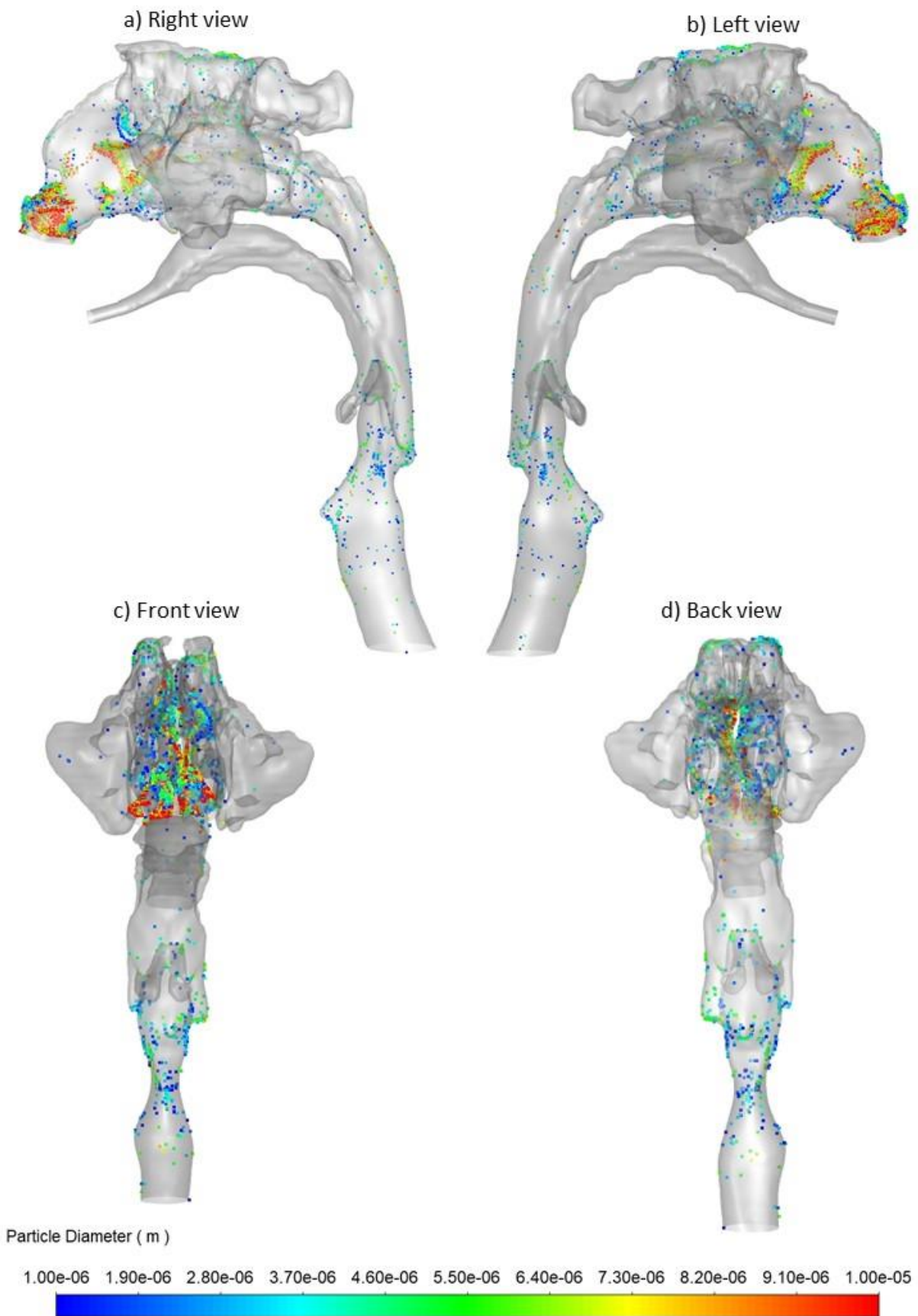


Figure 26: Particle deposition after nasal inhalation with 30 l/min.

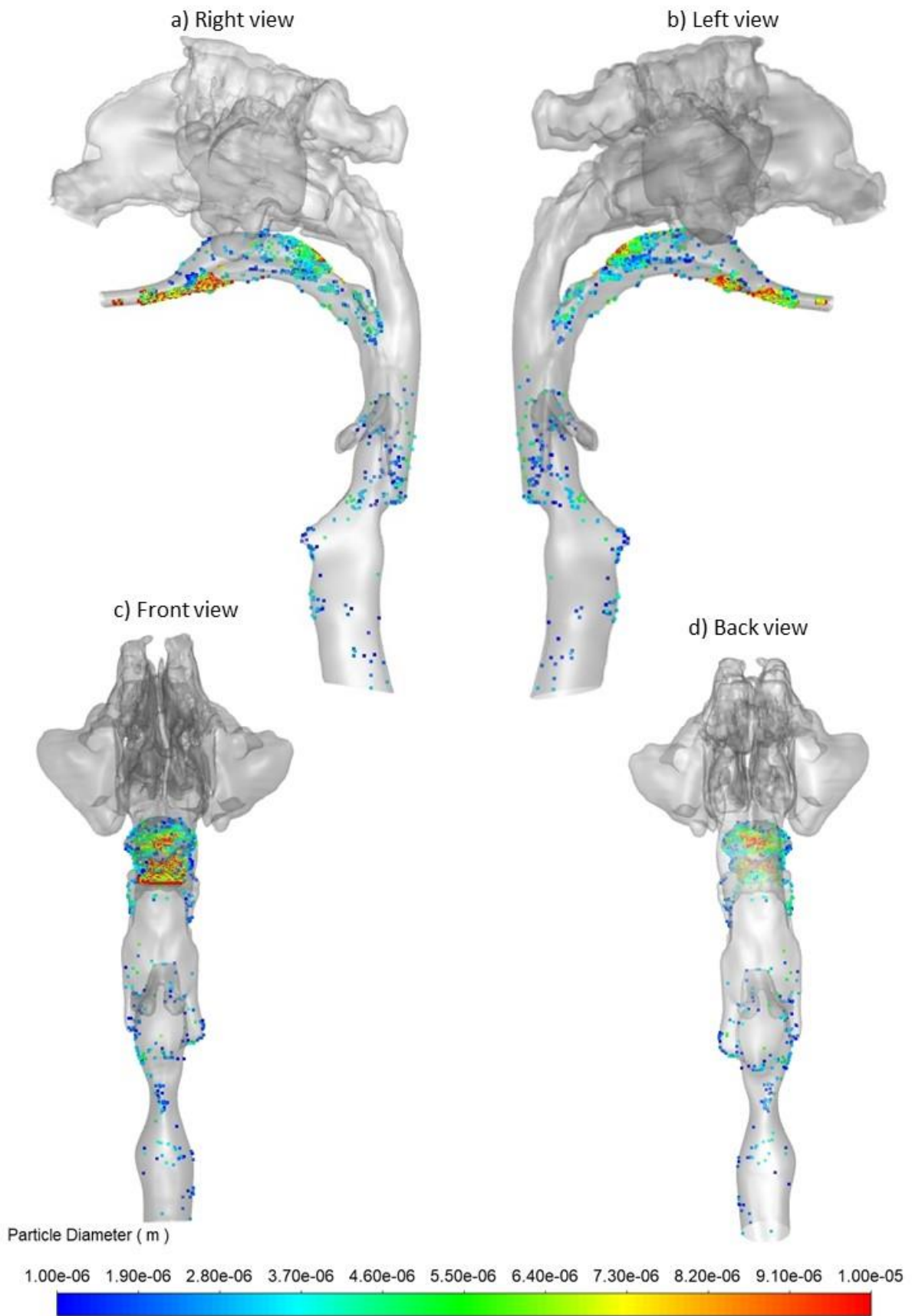


Figure 27: Particle deposition after oral inhalation with 90 l/min.

In Figure 28 it is evident that with flow rate of 15 l/min, there is high number of particles that escaped the URT (26 – 31 %). On the other hand, with flow rate 30 l/min, only 19 – 23 % of particles with the maximum diameter of 7 µm escaped (see Figure 29). The higher the initial velocity is, the more particles are captured in the nasal cavity. When we compare Figure 25 and Figure 26 we can notice with high initial velocity large particles with diameter (6-10 µm) are stuck in the nasal cavity and do not appear in laryngeal region, whereas with low velocity the more particles of 6-10 µm can be found in this region.

With oral inhalation (see Figure 27) the largest deposition of particles happened in C section, where deposited almost 35 % of total number of particles (see Figure 28). After this region, deposited particles significantly decreased in the following regions. We can notice in Figure 29 strange particle distribution during oral inhalation where there are no deposited particles in certain areas (2, 4, 6, 7, 9, 10 – in Figure 29). However, this pattern was observed in all 3 measurements. In the Figure 28 we can see that with oral inhalation the least particles (13 %) managed to escape from the URT, as opposed to nasal inhalation with flow rate 15l/min, where we measured the highest percentage (28 %)

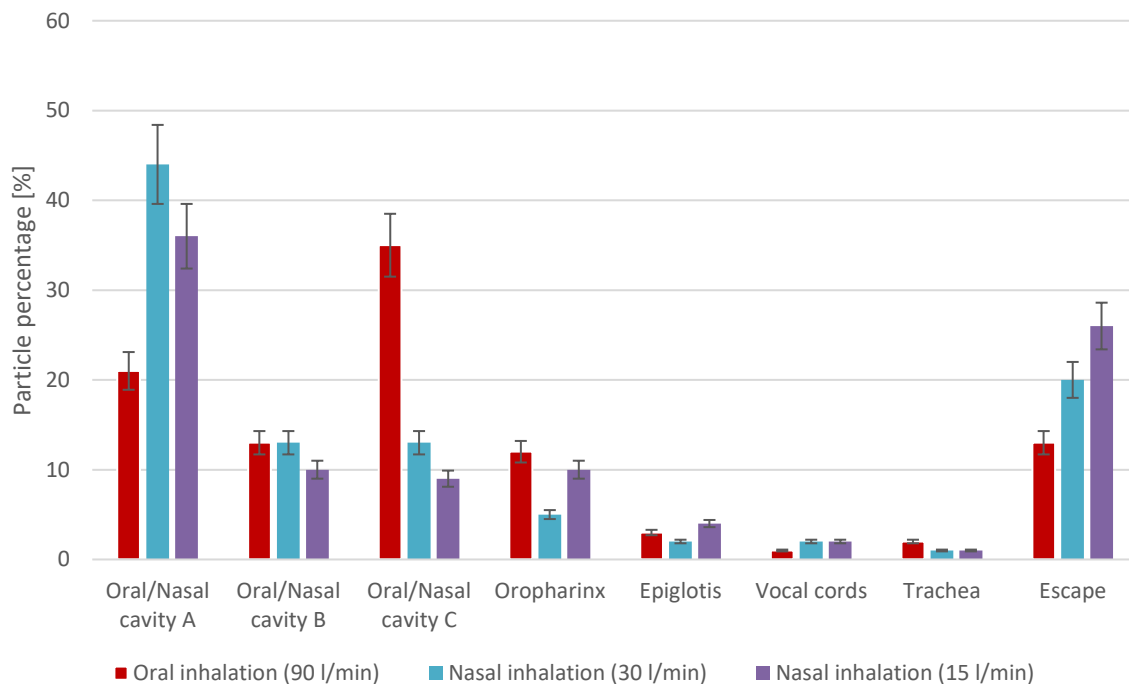


Figure 28: Particle percentage in different areas under various flow rates.

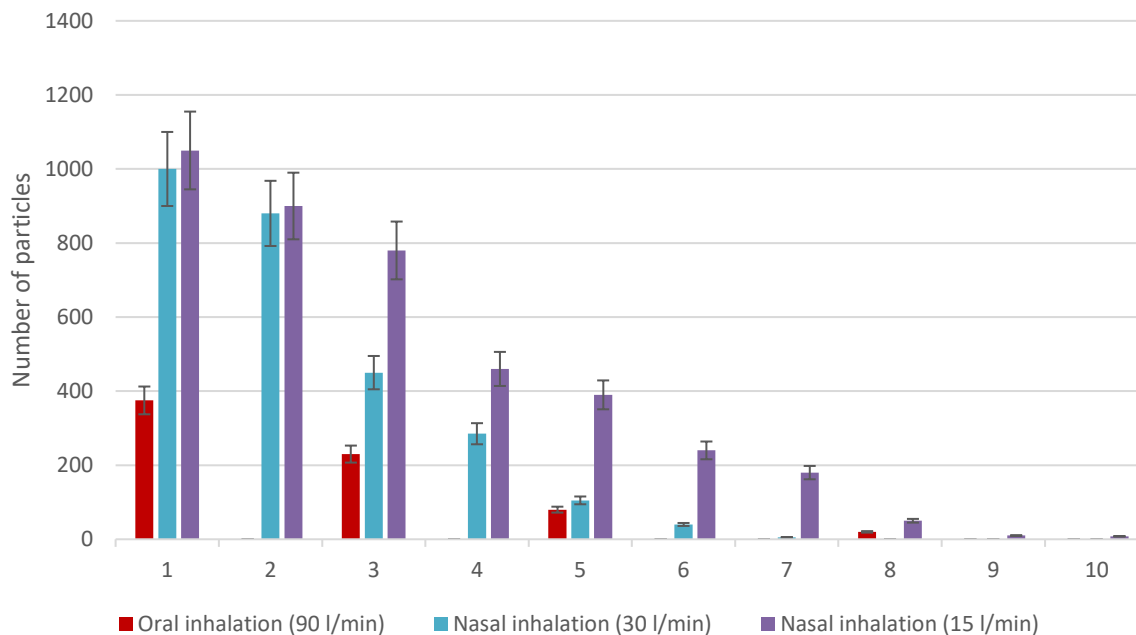


Figure 29: Comparison of outlet diameter distribution with various flow rates.

7 Discussion

Computational fluid dynamics has been recognized as a useful tool for understanding airflow characteristics in URT. The results can therefore advise us which particle distribution is the best choice for the treatment of certain diseases or can help us evaluate the therapy results when dealing with Sleep apnea-hypopnea syndrome.

In this study, a model of 20-year-old male model was used to simulate airflow values such as velocity, pressure, and particle deposition. The model represents the realistic geometry of the upper respiratory tract that was reconstructed from the CT scans to preserve all anatomical structures. It is known that even a small change in anatomy has a profound effect on the results. For example, first the model was examined with a connector for the air pump that was attached to the mouth, and the results were completely different as with the model that has a natural opening with the skin, as can be seen in the chapter 5.1.

Ansys 2020 was used as a leading program to evaluate the model. Ansys represents a package of SpaceClaim used for geometry modifications, and Fluent that is used for meshing and final computation. First Ansys 2021 student version was used. However, this version has big limitation where fluent can work with only 500 000 meshing elements whereas for proper meshing at least 3 000 000 was needed.

In the first place, such complex geometry needed to be adjusted because the model contained non-manifold geometry and overlapping regions. The model with these defects

cannot be meshed and in Fluent the error appears. Thus, SpaceClaim played a significant role in this work. At the beginning of the work, many simple models needed to be created in SpaceClaim to reveal how to solve these issues. After successful geometry adjustments, meshing can be initiated.

Meshing is used as a spatial discretization of the model and is a necessary step in CFD. Navier–Stokes equations are calculated for each element formed during meshing. The smaller the elements are, the more precise the solution is. But the computational complexity also increases. The best solution is to find a compromise between these two aspects. For this, we use the mesh independency test. This test helps us determine how many cells or elements will be sufficient for accurate results while keeping the computational complexity low. A mesh independency test was performed and eventually a mesh with 3 426 832 cells was used for further calculation.

An unstructured mesh was generated in Fluent, where hexahedral and polyhedral elements were used to create the mesh. Mesh contains polyhedral elements near the wall where it is not possible to create hexahedral. Hexahedral elements are on the other hand, formed in the middle of the fluid region. This type of mesh is called poly-hexcore. Another type of mesh that could be used with a similar quality is polyhedral. To create polyhedral elements fluent usually takes twice as much time (30 minutes) as creating poly-hexcore (15 minutes). However, poly-hexcore is sometimes difficult to create if the geometry is too complex or with some defects. In this case, fluent after meshing process, which can take 15 minutes, shows an error, indicating that he was not successful in generating the mesh. After this, it is necessary to start the meshing process again with a little change in element size.

LES method was used to calculate the solution when dealing with laminar-turbulent flows. Although it is very computationally demanding, it provides very accurate results. Calculation of one solution took approximately 60 hours. However, calculation duration is highly dependent on the time steps selected at the beginning of the calculation in the fluent settings. If we select a large time step, the calculation takes less time, but we don't see the time development of particle distribution in animation. Furthermore, for the sake of precision, it is recommended to select a shorter time step. Also, other viscous models like SST transition and SST k-omega were examined. With these models, computation is much faster than with LES, yet the results are not that precise.

When we compare the results with Liu et al. (2022) mentioned in 4.2, which is nowadays the latest article made on URT exploration, we can notice very similar velocity contours in nasal inhalation with a flow rate of 15 and 30 l/min. There are some similarities, such as a higher velocity in one nostril. Also, there is a gradual increase in velocity from the oropharynx up to the vocal cords. However, there are some differences. In contours by Liu et al. (2022), the velocity doesn't decrease after the subglottis region, whereas the contour in this thesis shows a significant fall in velocity magnitude. When we look at the maximum velocity, we can

notice another dissimilarity because in contours by Liu et al. (2022), the maximum velocity is twice as high as in this thesis. This can be caused by greater narrowing of the nostrils.

When we focus more on the pressure contours, the most significant feature is the pressure drop in the laryngeal region. Not many studies were conducted on the pressure investigation of URT. Although there are studies on the tracheobronchial region and how the pressure changes in bifurcations. However, it was discovered that pressure drop occurs as a result of a rapid change in velocity. A change in velocity occurs due to a sudden narrowing in geometry.

With closer look to particle deposition, we can see consistent results with the study conducted by Naseri et al. (2014) and Liu et al. (2022), closer described in in chapter 4.2. The particles of a diameter 1-5 μm are most likely to escape from URT. The particles of a diameter 6-10 μm are mostly stuck in the nasal or oral cavity during medicament inhalation. It is observed that the particle deposition is highly dependent on the flow rate. In Figure 30 we can notice that Liu et al. observed higher particle deposition in nasal cavity in both flowrates than in this thesis. Fewer particles escape from URT in Liu et al. study. Particle deposition in Pharynx and Larynx are comparable.

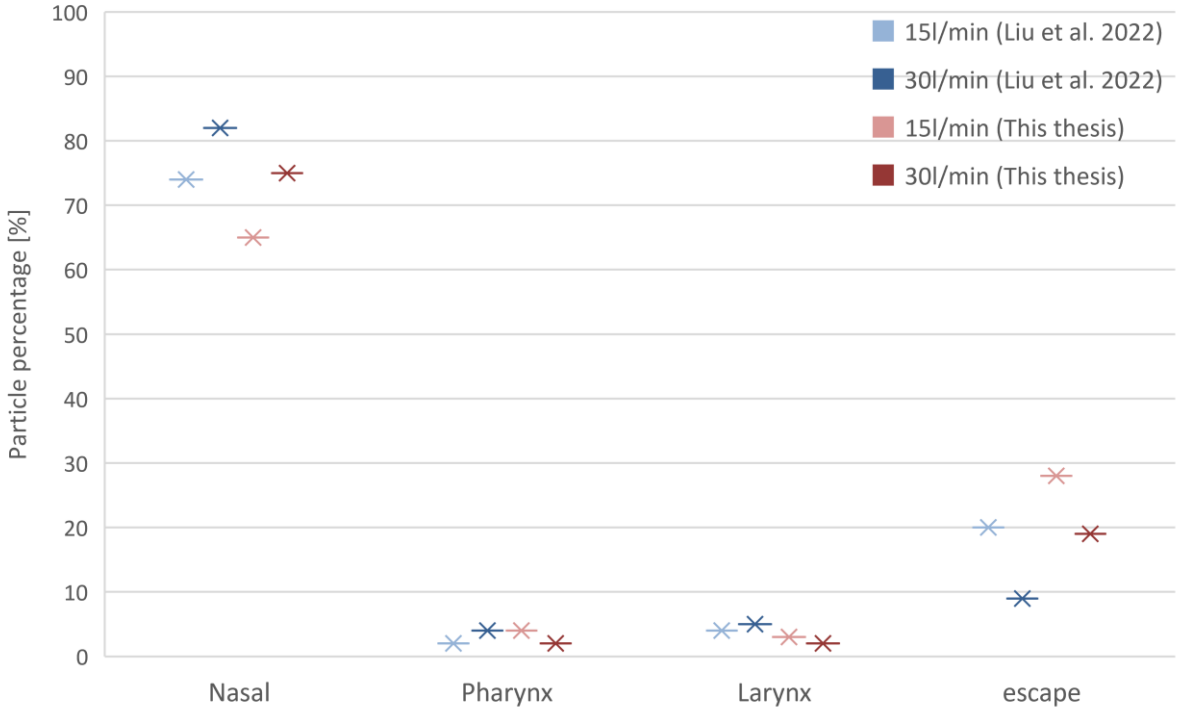


Figure 30: Comparison of particle deposition with Liu et al. (2022) during nasal inhalation.

Naseri et al. (2014) in his research used flow rate of 7 l/min and even 10 μm particles were evenly distributed in the whole URT which wasn't observed in this thesis because minimum flow rate was 15 l/min.

A proposal for future work could be to extend the URT also to the lower respiratory tract. Another extension could be to use exhalation/ inhalation breathing pattern to better predict behavior of particles during inhalation therapy.

8 Conclusion

The flow characteristics and particle deposition in the upper respiratory tract of 20-year-old male were successfully simulated using ANSYS software. All the results can be found in chapter 6. Starting from velocity and pressure contours and ending with particle deposition in different cross sections. Flow patterns and particle depositions in this work are comparable with other research conducted on profound understanding of the respiratory tract. Velocity contours are in accordance with Liu et al. (2022) depicted in Figure 9. And particle distribution of different flow rates is also very similar with Figure 11.

It was observed that particle deposition in URT is highly dependent on particle diameter distribution and the flow rate used for inhalation. CFD simulations can advise us what parameters to use for the treatment of particular illness. In this work it was found that the most suitable particle diameter ranges between 1-10 μm . When the particles are larger, they tend to be stuck at the beginning of URT and thus are not suitable for deeper inhalation therapy.

The setup process and methods used in this thesis may be applicable for further research on URT under different conditions, which can include anatomical changes in various diseases like asthma or other forms of obstructions.

Bibliography

- [1] N. Khaltaev and S. Axelrod, "Chronic respiratory diseases global mortality trends, treatment guidelines, life style modifications, and air pollution: preliminary analysis," *J. Thorac. Dis.*, vol. 11, no. 6, p. 2643, Jun. 2019, doi: 10.21037/JTD.2019.06.08.
- [2] "Global Burden of Disease: GBD cause and risk summaries." <https://www.thelancet.com/gbd/summaries> (accessed May 11, 2022).
- [3] J. B. Soriano *et al.*, "Prevalence and attributable health burden of chronic respiratory diseases, 1990–2017: a systematic analysis for the Global Burden of Disease Study 2017," *Lancet. Respir. Med.*, vol. 8, no. 6, p. 585, Jun. 2020, doi: 10.1016/S2213-2600(20)30105-3.
- [4] S. Festing and R. Wilkinson, "The ethics of animal research. Talking Point on the use of animals in scientific research," *EMBO Rep.*, vol. 8, no. 6, p. 526, Jun. 2007, doi: 10.1038/SJ.EMBOR.7400993.
- [5] L. Matthiessen, B. Lucaroni, and E. Saez, "Towards responsible animal research," *EMBO Rep.*, vol. 4, no. 2, p. 104, Feb. 2003, doi: 10.1038/SJ.EMBOR.EMBOR745.
- [6] J. HYNES *et al.*, "Advanced Non-animal Models in Biomedical Research," pp. 1–88, 2020, doi: 10.2760/725821.
- [7] R. Pasteka, L. A. Schöllbauer, J. P. S. da Costa, R. Kolar, and M. Forjan, "Experimental Evaluation of Dry Powder Inhalers during Inhalation and Exhalation Using a Model of the Human Respiratory System (xPULM™)," *Pharm. 2022, Vol. 14, Page 500*, vol. 14, no. 3, p. 500, Feb. 2022, doi: 10.3390/PHARMACEUTICS14030500.
- [8] D. Shier, B. Jackie, and L. Ricki, *Hole's Essentials of Human Anatomy and Physiology*, 12th ed. 2018.
- [9] A. Mete and İ. H. Akbudak, "Functional Anatomy and Physiology of Airway," *Tracheal Intubation*, Jul. 2018, doi: 10.5772/INTECHOPEN.77037.
- [10] L. Adewale, "Anatomy and assessment of the pediatric airway," *Paediatr. Anaesth.*, vol. 19 Suppl 1, no. SUPPL. 1, pp. 1–8, Jul. 2009, doi: 10.1111/J.1460-9592.2009.03012.X.
- [11] P. Pohunek, "Development, structure and function of the upper airways," *Paediatr. Respir. Rev.*, vol. 5, no. 1, pp. 2–8, 2004, doi: 10.1016/J.PRRV.2003.09.002.
- [12] D. R. Hess and R. Faarc, "Respiratory Mechanics in Mechanically Ventilated Patients," *Respir. Care*, vol. 59, no. 11, pp. 1773–1794, Nov. 2014, doi: 10.4187/RESPCARE.03410.
- [13] U. Lucangelo, F. Bernabè, and L. Blanch, "Lung mechanics at the bedside: make it simple," *Curr. Opin. Crit. Care*, vol. 13, no. 1, pp. 64–72, Feb. 2007, doi: 10.1097/mcc.0b013e32801162df.
- [14] M. G. Levitzky, "Using the pathophysiology of obstructive sleep apnea to teach cardiopulmonary integration," *Am. J. Physiol. - Adv. Physiol. Educ.*, vol. 32, no. 3, pp.

- 196–202, 2008, doi: 10.1152/ADVAN.90137.2008.
- [15] B. Song *et al.*, “Computational fluid dynamics simulation of changes in the morphology and airflow dynamics of the upper airways in OSAHS patients after treatment with oral appliances,” *PLoS One*, vol. 14, no. 11, p. e0219642, Nov. 2019, doi: 10.1371/JOURNAL.PONE.0219642.
- [16] K. Coyne, D. Caretti, W. Scott, A. Johnson, and F. Koh, “Inspiratory Flow Rates During Hard Work When Breathing Through Different Respirator Inhalation and Exhalation Resistances,” <http://dx.doi.org/10.1080/15459620600867807>, vol. 3, no. 9, pp. 490–500, Sep. 2009, doi: 10.1080/15459620600867807.
- [17] X. Wei *et al.*, “In vitro tests for aerosol deposition. VI: Realistic testing with different mouth-throat models and in vitro - In vivo correlations for a dry powder inhaler, metered dose inhaler, and soft mist inhaler,” *J. Aerosol Med. Pulm. Drug Deliv.*, vol. 31, no. 6, pp. 358–371, Dec. 2018, doi: 10.1089/JAMP.2018.1454/ASSET/IMAGES/LARGE/FIGURE6.JPEG.
- [18] J. G. Speight, “Sources and Types of Organic Pollutants,” *Environ. Org. Chem. Eng.*, pp. 153–201, Jan. 2017, doi: 10.1016/B978-0-12-804492-6.00004-6.
- [19] M. B. Dolovich *et al.*, “Device selection and outcomes of aerosol therapy: Evidence-based guidelines: American College of Chest Physicians/American College of Asthma, Allergy, and Immunology,” *Chest*, vol. 127, no. 1, pp. 335–371, 2005, doi: 10.1378/CHEST.127.1.335.
- [20] M. L. Levy, W. Carroll, J. L. Izquierdo Alonso, C. Keller, F. Lavorini, and L. Lehtimäki, “Understanding Dry Powder Inhalers: Key Technical and Patient Preference Attributes,” *Adv. Ther.*, vol. 36, no. 10, p. 2547, Oct. 2019, doi: 10.1007/S12325-019-01066-6.
- [21] “(16) (PDF) Comparing clinical features of the nebulizer, metered-dose inhaler, and dry powder inhaler.” https://www.researchgate.net/publication/7579746_Comparing_clinical_features_of_the_nebulizer_metered-dose_inhaler_and_dry_powder_inhaler (accessed Aug. 22, 2022).
- [22] S. Smith, N. J. Rowbotham, and K. H. Regan, “Inhaled anti-pseudomonal antibiotics for long-term therapy in cystic fibrosis,” *Cochrane Database Syst. Rev.*, vol. 2018, no. 3, Mar. 2018, doi: 10.1002/14651858.CD001021.PUB3.
- [23] L. Borgström, “On the use of dry powder inhalers in situations perceived as constrained,” *J. Aerosol Med.*, vol. 14, no. 3, pp. 281–287, 2001, doi: 10.1089/089426801316970231.
- [24] Y. S. Cheng, “Mechanisms of Pharmaceutical Aerosol Deposition in the Respiratory Tract,” *AAPS PharmSciTech*, vol. 15, no. 3, p. 630, 2014, doi: 10.1208/S12249-014-0092-0.
- [25] M. M. Rahman, M. Zhao, M. S. Islam, K. Dong, and S. C. Saha, “Aerosol Particle Transport and Deposition in Upper and Lower Airways of Infant, Child and Adult Human Lungs,” *Atmos. 2021, Vol. 12, Page 1402*, vol. 12, no. 11, p. 1402, Oct. 2021, doi: 10.3390/ATMOS12111402.
- [26] Gillina Bezemer, “Particle deposition and clearance from the respiratory tract,” 2009.

- [27] Q. Deng, L. Deng, Y. Miao, X. Guo, and Y. Li, "Particle deposition in the human lung: Health implications of particulate matter from different sources," *Environ. Res.*, vol. 169, pp. 237–245, Feb. 2019, doi: 10.1016/J.ENVRES.2018.11.014.
- [28] Z. Zhang, C. Kleinstreuer, C. S. Kim, and Y. S. Cheng, "Vaporizing Microdroplet Inhalation, Transport, and Deposition in a Human Upper Airway Model," <http://dx.doi.org/10.1080/02786820490247597>, vol. 38, no. 1, pp. 36–49, Jan. 2010, doi: 10.1080/02786820490247597.
- [29] A. Tsuda, F. S. Henry, and J. P. Butler, "Particle Transport and Deposition: Basic Physics of Particle Kinetics," *Compr. Physiol.*, vol. 3, no. 4, pp. 1437–1471, 2013, doi: 10.1002/CPHY.C100085.
- [30] C. Darquenne, "Aerosol Deposition in Health and Disease," *J. Aerosol Med. Pulm. Drug Deliv.*, vol. 25, no. 3, p. 140, Jun. 2012, doi: 10.1089/JAMP.2011.0916.
- [31] A. H. L. Chow, H. H. Y. Tong, P. Chattopadhyay, and B. Y. Shekunov, "Particle engineering for pulmonary drug delivery," *Pharm. Res.*, vol. 24, no. 3, pp. 411–437, Mar. 2007, doi: 10.1007/S11095-006-9174-3/TABLES/3.
- [32] N. Stevens and D. Prime, "Drug Delivery to the Lungs 26, 2015 – N Stevens et al. How Particle Size Changes Lung Deposition: A Physical Modeller's Perspective," 2015.
- [33] P. Koullapis *et al.*, "Regional aerosol deposition in the human airways: The SimInhale benchmark case and a critical assessment of in silico methods," *Eur. J. Pharm. Sci.*, vol. 113, pp. 77–94, Feb. 2018, doi: 10.1016/J.EJPS.2017.09.003.
- [34] F. Moukalled, L. Mangani, and M. Darwish, "The Finite Volume Method in Computational Fluid Dynamics," vol. 113, 2016, doi: 10.1007/978-3-319-16874-6.
- [35] S. Jamshed, "Introduction to CFD," *Using HPC Comput. Fluid Dyn.*, pp. 1–20, 2015, doi: 10.1016/B978-0-12-801567-4.00001-5.
- [36] P. Das, E. Nof, I. Amirav, S. C. Kassinos, and J. Sznitman, "Targeting inhaled aerosol delivery to upper airways in children: Insight from computational fluid dynamics (CFD)," *PLoS One*, vol. 13, no. 11, Nov. 2018, doi: 10.1371/JOURNAL.PONE.0207711.
- [37] X. Cui, W. Wu, and H. Ge, "Investigation of airflow field in the upper airway under unsteady respiration pattern using large eddy simulation method," *Respir. Physiol. Neurobiol.*, vol. 279, p. 103468, Aug. 2020, doi: 10.1016/J.RESP.2020.103468.
- [38] Y. Zhiyin, "Large-eddy simulation: Past, present and the future," *Chinese J. Aeronaut.*, vol. 28, no. 1, pp. 11–24, Feb. 2015, doi: 10.1016/J.CJA.2014.12.007.
- [39] X. Xu, J. Wu, W. Weng, and M. Fu, "Investigation of inhalation and exhalation flow pattern in a realistic human upper airway model by PIV experiments and CFD simulations," *Biomech. Model. Mechanobiol.*, vol. 19, no. 5, pp. 1679–1695, Oct. 2020, doi: 10.1007/S10237-020-01299-3/FIGURES/13.
- [40] A. Naseri, O. Abouali, P. F. Ghalati, and G. Ahmadi, "Numerical investigation of regional particle deposition in the upper airway of a standing male mannequin in calm air surroundings," *Comput. Biol. Med.*, vol. 52, pp. 73–81, Sep. 2014, doi: 10.1016/J.COMPBIOMED.2014.06.007.

- [41] W. Liu, Y. Wu, G. Liu, and H. Lu, "Study on the multi-component particle-gas two-phase flow in a human upper respiratory tract," *Powder Technol.*, vol. 397, p. 117030, Jan. 2022, doi: 10.1016/J.POWTEC.2021.117030.
- [42] M. Rahiminejad, A. Haghghi, A. Dastan, O. Abouali, M. Farid, and G. Ahmadi, "Computer simulations of pressure and velocity fields in a human upper airway during sneezing," *Comput. Biol. Med.*, vol. 71, pp. 115–127, Apr. 2016, doi: 10.1016/J.COMPBIOMED.2016.01.022.
- [43] J. D. Anderson, "Governing Equations of Fluid Dynamics," *Comput. Fluid Dyn.*, pp. 15–51, 1992, doi: 10.1007/978-3-662-11350-9_2.
- [44] V. K. H. Bui, J. Y. Moon, M. Chae, D. Park, and Y. C. Lee, "Prediction of Aerosol Deposition in the Human Respiratory Tract via Computational Models: A Review with Recent Updates," *Atmos. 2020, Vol. 11, Page 137*, vol. 11, no. 2, p. 137, Jan. 2020, doi: 10.3390/ATMOS11020137.
- [45] "ANSYS FLUENT 12.0 Theory Guide - 15.2.1 Equations of Motion for Particles." <https://www.afs.enea.it/project/neptunius/docs/fluent/html/th/node241.htm> (accessed May 12, 2022).
- [46] M. Sosnowski, J. Krzywanski, K. Grabowska, and R. Gnatowska, "Polyhedral meshing in numerical analysis of conjugate heat transfer," *EPJ Web Conf.*, vol. 180, p. 02096, 2018, doi: 10.1051/EPJCONF/201818002096.

List of Figures

Figure 1: Anatomy of the upper respiratory tract [8].	7
Figure 2: Changes in lung volume, alveolar pressure, pleural pressure and transpulmonary pressure during normal breathing [14].	10
Figure 3: Different mechanisms of particle deposition [26].	13
Figure 4: Particle deposition in lungs with three different types [27].	13
Figure 5: Lung deposition distribution for various particle sizes [32].	15
Figure 6: realistic extra-thoracic region developed by Naseri et al. (2014) [40].	19
Figure 7: deposition pattern variation by particle size with flow rate of 7 l/min [40].	20
Figure 8: Realistic model of URT with cross sections by Liu et al. (2022) [41].	20
Figure 9: Velocity distribution in different cross-sections by Liu et al. (2022) [41].	21
Figure 10: Distribution map of different particle sizes by Liu et al. (2022) [41].	22
Figure 11: Particle distribution for different sizes by Liu et al. (2022) [41].	22
Figure 12: Schematic of geometry utilized by Rahiminejad and his team (2016) [42].	23
Figure 13: 2D velocity magnitude contours for the flow rate of 470 l/min [42].	23
Figure 14: Model preview and Selected sections of the CFD model by Song et al. (2019) [15].	24
Figure 15: Model preview from four different sides.	25
Figure 16: Difference between the filtered velocity u_i and the instantaneous velocity u_x [38].	26
Figure 17: 3D mesh model of the upper airways with poly-hexcore unstructured mesh.	33
Figure 18: Cross sections in transverse and longitudinal direction.	36
Figure 19: Velocity contours with flow rate of 15 l/min.	37
Figure 20: Velocity contours with flow rate of 30 l/min.	38
Figure 21: Velocity contours with flow rate of 90 l/min.	39
Figure 22: Pressure contours with flow rate of 15 l/min.	40
Figure 23: Pressure contours with flow rate of 30 l/min.	41
Figure 24: Pressure contours with flow rate of 90 l/min.	42
Figure 25: Particle deposition after nasal inhalation with 15 l/min.	44
Figure 26: Particle deposition after nasal inhalation with 30 l/min.	45

Figure 27: Particle deposition after oral inhalation with 90 l/min.....	46
Figure 28: Particle percentage in different areas under various flow rates.....	47
Figure 29: Comparison of outlet diameter distribution with various flow rates.....	48
Figure 30: Comparison of particle deposition with Liu et al. (2022) during nasal inhalation...50	
Figure 31: Turbulent kinetic energy during the oral inhalation (90 l/min). Turbulent kinetic energy is in LES method represented by Subgrid turbulent viscosity.....	61
Figure 32: Turbulent kinetic energy during the nasal inhalation (30 l/min). Turbulent kinetic energy is in LES method represented by Subgrid turbulent viscosity.....	62
Figure 33: Turbulent kinetic energy during the nasal inhalation (15 l/min). Turbulent kinetic energy is in LES method represented by Subgrid turbulent viscosity.....	62
Figure 34: Wall sheer stress during the oral inhalation (90 l/min).....	63
Figure 35: Wall sheer stress during the nasal inhalation (30 l/min).	64
Figure 36: Wall sheer stress during the nasal inhalation (15 l/min).	65

List of Tables

Table 1: Fluent setting used during computation	35
Table 2: Particle percentage in different areas of URT with nasal inhalation (15 l/min).....	60
Table 3: Particle percentage in different areas of URT with nasal inhalation (30 l/min).....	60
Table 4: Particle percentage in different areas of URT with oral inhalation (90 l/min).	60

List of Abbreviations

URT	Upper Respiratory Tract
CT	Computed Tomography
MRI	magnetic resonance imaging
CFD	Computational Fluid Dynamics
FD	Fluid Dynamics
DPM	Discrete Phase Model
3D	Three-Dimensional
2D	Two-Dimensional
DPI	Dry Powder Inhalers
MDI	Metered Dose Inhaler
LES	Large Eddy Simulation
DNS	Direct Numerical Simulation
RANS	Reynolds Averaged Navier Stokes
COPD	Chronic obstructive pulmonary disease
FEM	Finite Element Method
FDM	Finite Difference Method
FVM	Finite Volume Method
DICOM	Digital Imaging and Communications in Medicine
STL	Standard Triangle Language

Appendix A: Variability in Particle Deposition

Table 2: Particle percentage in different areas of URT with nasal inhalation (15 l/min).

	Nasal cavity A [%]	Nasal cavity B [%]	Nasal cavity C [%]	Oropharynx [%]	Epiglottis [%]	Vocal cords [%]	Trachea [%]	Escape [%]
1. measurement	36	10	9	10	4	2	1	28
2. measurement	36	9	10	9	5	2	1	28
3. measurement	40	12	9	8	3	2	1	25

Table 3: Particle percentage in different areas of URT with nasal inhalation (30 l/min).

	Nasal cavity A [%]	Nasal cavity B [%]	Nasal cavity C [%]	Oropharynx [%]	Epiglottis [%]	Vocal cords [%]	Trachea [%]	Escape [%]
1. measurement	44	13	13	5	2	2	1	20
2. measurement	48	15	11	4	1	1	1	19
3. measurement	40	15	15	3	1	2	1	23

Table 4: Particle percentage in different areas of URT with oral inhalation (90 l/min).

	Nasal cavity A [%]	Nasal cavity B [%]	Nasal cavity C [%]	Oropharynx [%]	Epiglottis [%]	Vocal cords [%]	Trachea [%]	Escape [%]
1. measurement	21	13	35	12	3	1	2	13
2. measurement	18	14	39	10	2	2	1	14
3. measurement	22	15	38	10	2	1	1	11

Appendix B: Turbulent Kinetic Energy Contours

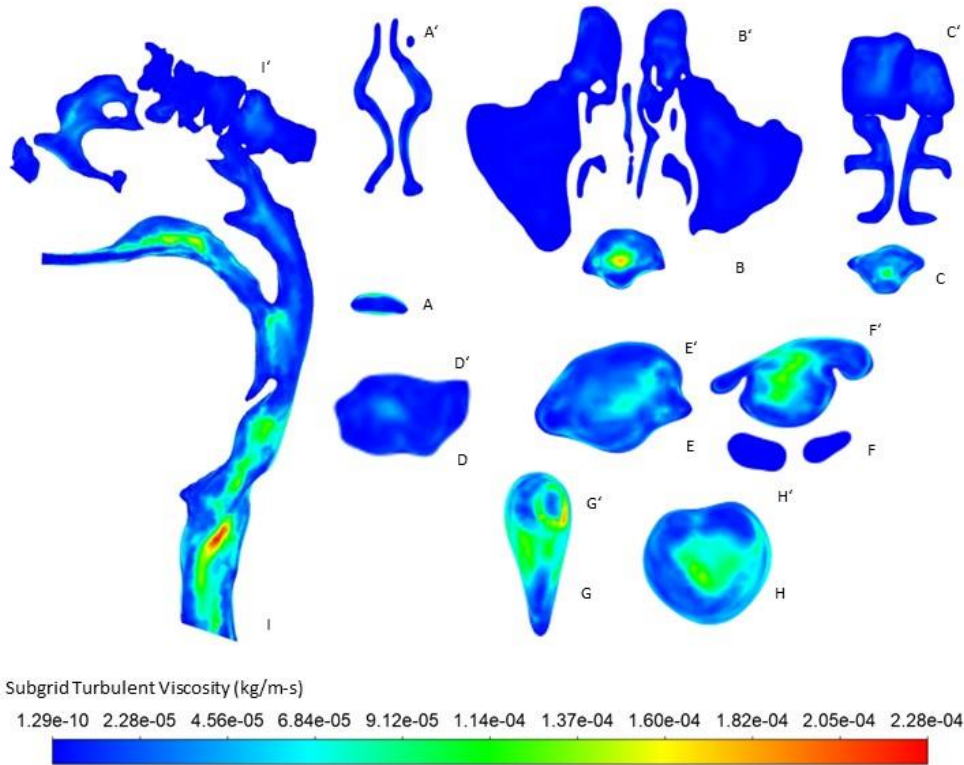


Figure 31: Turbulent kinetic energy during the oral inhalation (90 l/min). Turbulent kinetic energy is in LES method represented by Subgrid turbulent viscosity.

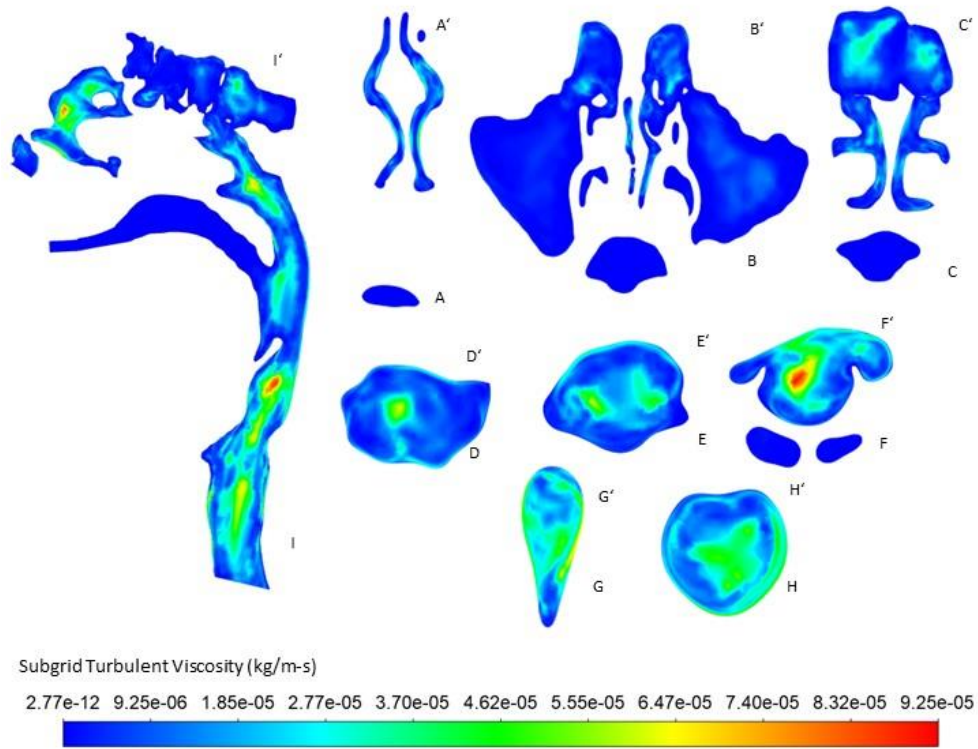


Figure 32: Turbulent kinetic energy during the nasal inhalation (30 l/min). Turbulent kinetic energy is in LES method represented by Subgrid turbulent viscosity.

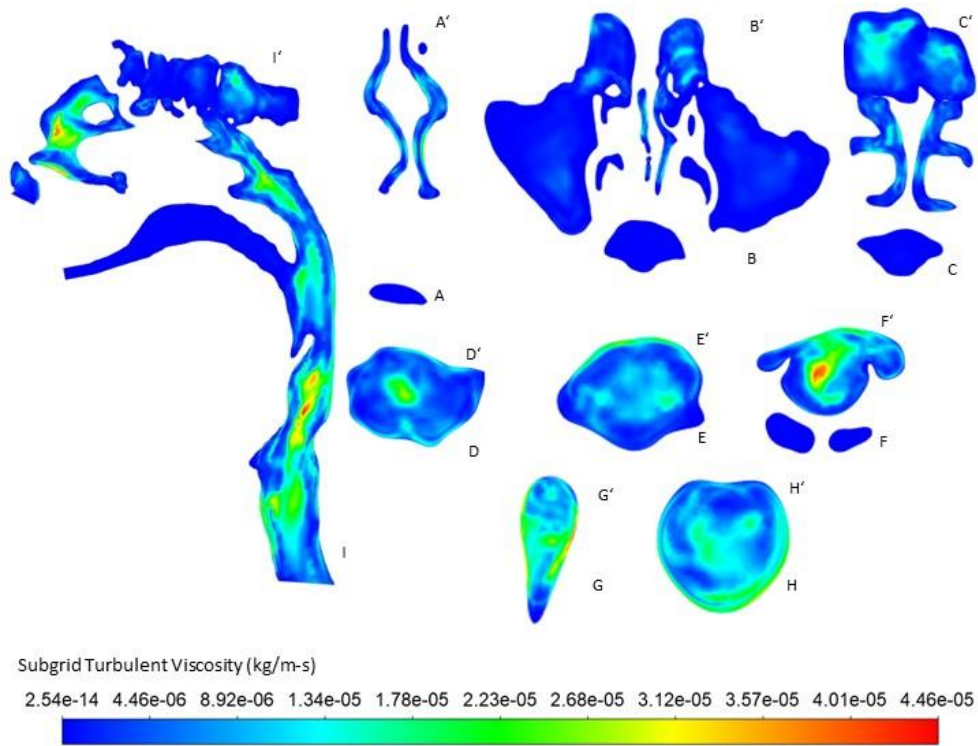


Figure 33: Turbulent kinetic energy during the nasal inhalation (15 l/min). Turbulent kinetic energy is in LES method represented by Subgrid turbulent viscosity.

Appendix C: Wall Shear Stress

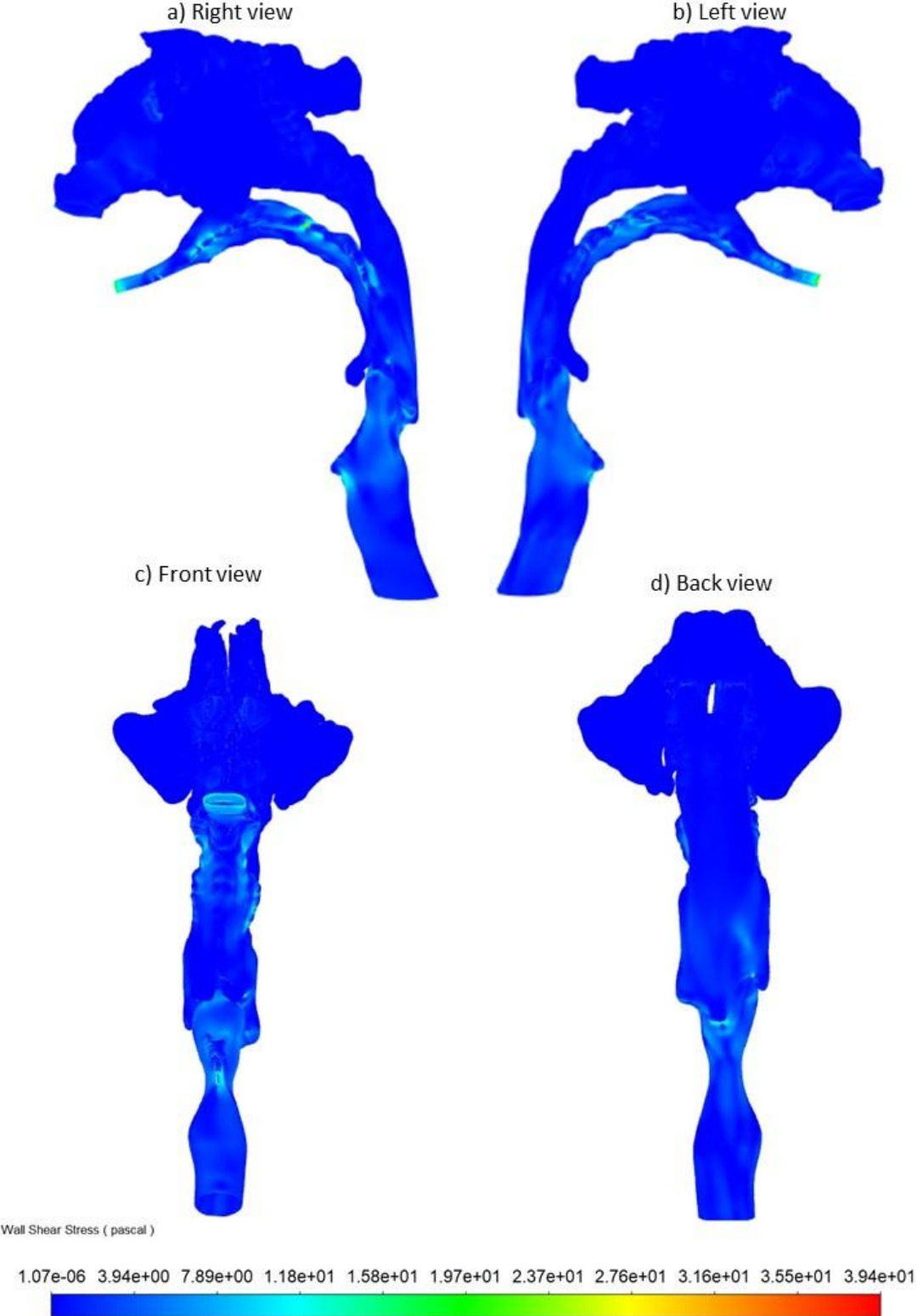


Figure 34: Wall shear stress during the oral inhalation (90 l/min)

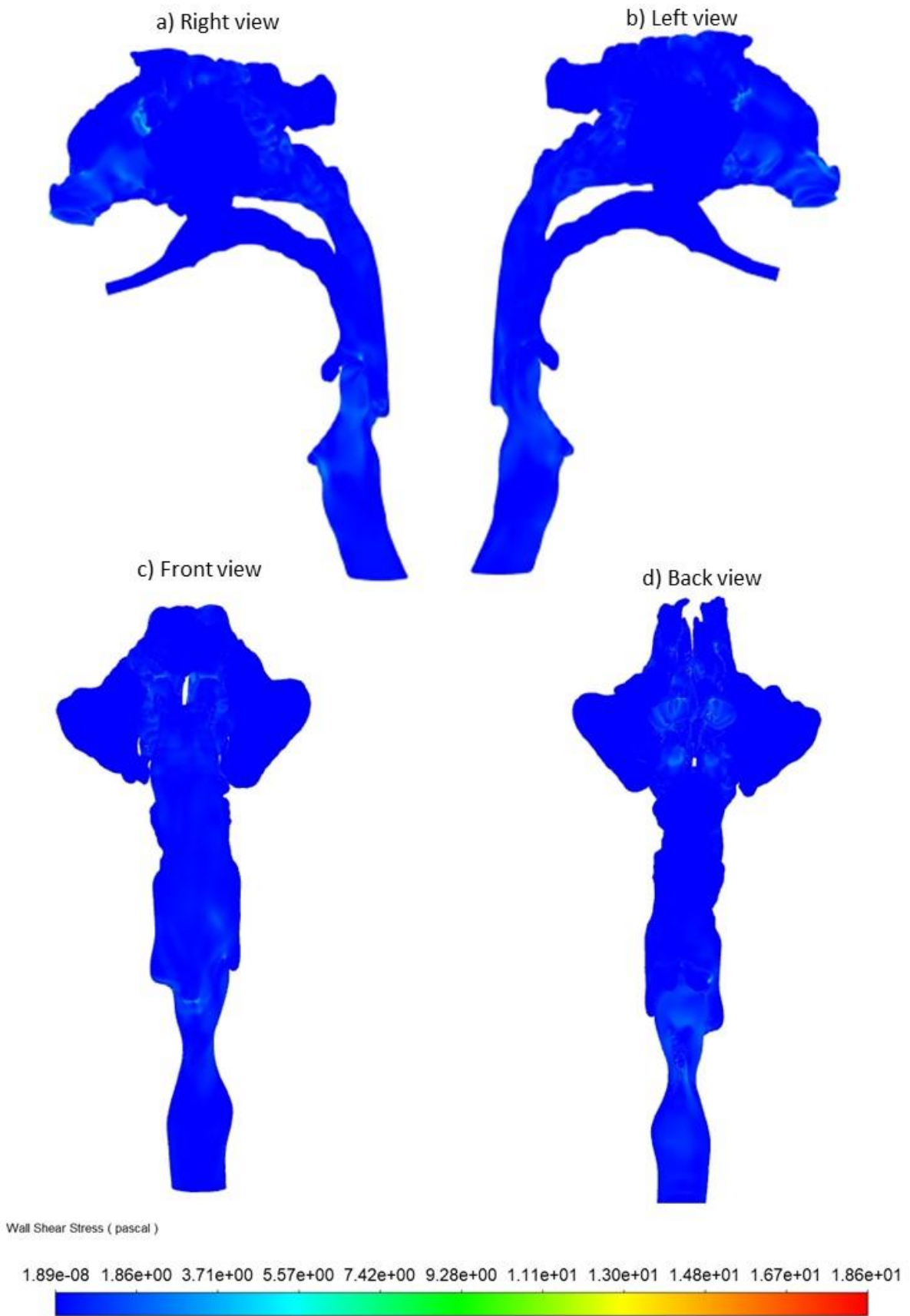


Figure 35: Wall sheer stress during the nasal inhalation (30 l/min).

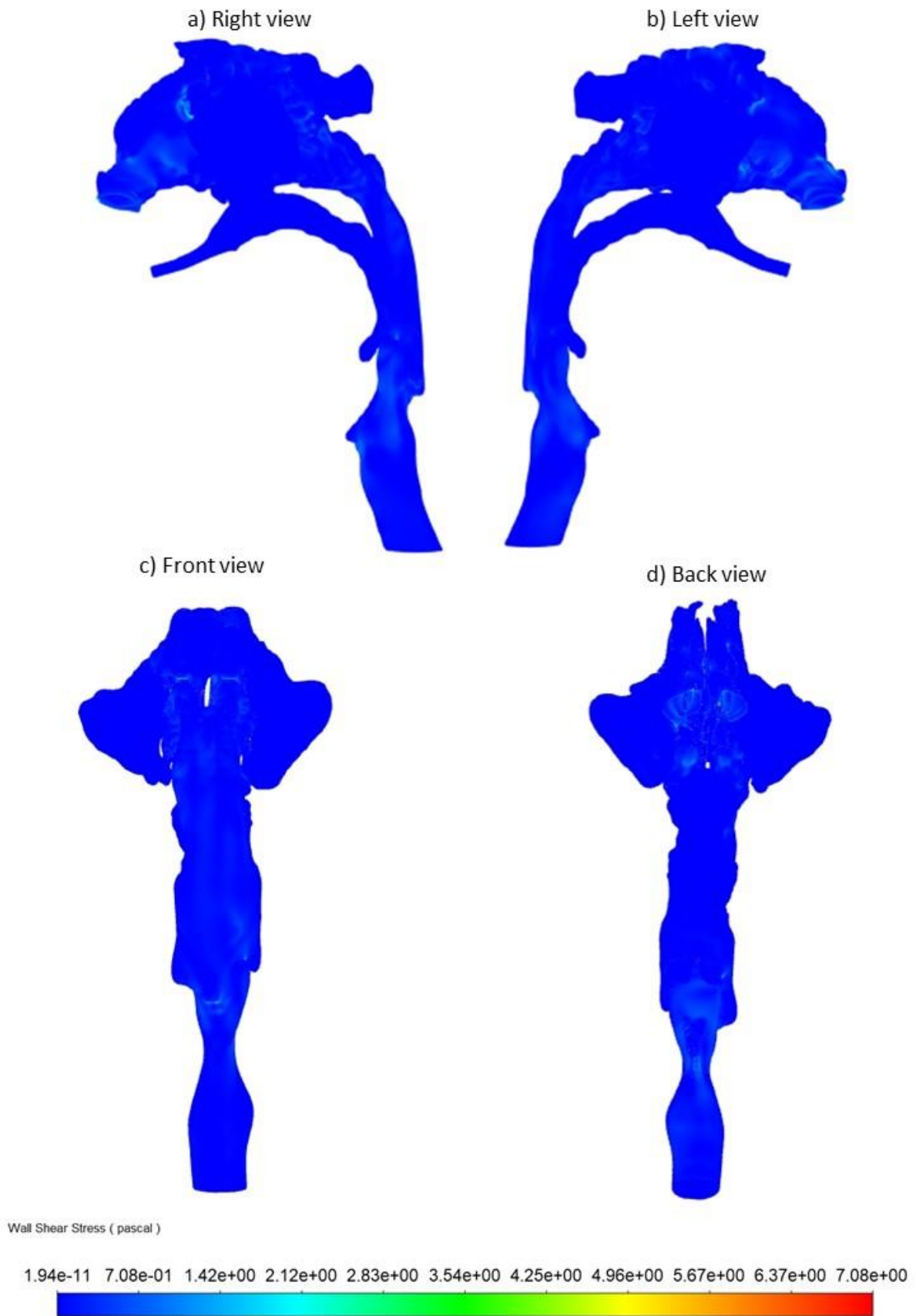


Figure 36: Wall shear stress during the nasal inhalation (15 l/min).